Supplementary Information

to

Novel Stable Ytterbium Acetylacetonate-Quinaldinate Complexes as Single-Molecule Magnets and Surprisingly Efficient Luminophores

by

Andrey V. Gavrikov[a], Andrey B. Ilyukhin[a], Ilya V. Taydakov[b],
Mikhail T. Metlin[b,c], Nikolay P.Datskevich[b],
Mikhail E. Buzoverov[a], Konstantin A. Babeshkin[a], Nikolay N. Efimov[a]

Table S1. Crystal data and structure refinement for **1**, **2**, **2_1**.

Identification code	**1**	**2**	**2_1**
Empirical formula	$C_{20}H_{20}NO_6Yb$	$C_{32}H_{28}N_3O_6Yb$	$C_{35}H_{37}N_3O_{7.50}Yb$
Formula weight	543.41	723.61	792.71
Temperature, K	100(2)	150(2)	100(2)
Wavelength, Å	0.71073	0.71073	0.71073
Crystal system	Monoclinic	Triclinic	Triclinic
Space group	$P2_1/n$	P-1	P-1
a, Å	9.3312(2)	10.1267(4)	11.9925(4)
b, Å	11.6285(3)	12.5770(5)	12.1587(4)
c, Å	18.2162(5)	12.5907(5)	26.1155(8)
α, °	90	83.2460(10)	101.6180(10)
β, °	96.5070(10)	71.9510(10)	92.0670(10)
γ, °	90	67.4820(10)	118.4930(10)
Volume, $Å^3$	1963.87(9)	1408.44(10)	3239.33(18)
Z	4	2	4
D (calc), Mg/m^3	1.838	1.706	1.625
μ, mm^{-1}	4.798	3.371	2.942
F(000)	1060	718	1592
Crystal size, mm	0.28 x 0.20 x 0.18	0.28 x 0.22 x 0.20	0.20 x 0.12 x 0.04
θ range, °	2.082, 36.130	2.274, 30.138	2.057, 33.159
Index ranges	-14<=h<=14 -17<=k<=18 -28<=l<=28	-13<=h<=14 -16<=k<=17 -17<=l<=17	-18<=h<=18 -18<=k<=18 -37<=l<=40
Reflections collected	43043	30295	97701
Independent reflections, Rint	8524, 0.0364	7753, 0.0561	23599, 0.0284
Completeness to θ = 25.242°	99.9 %	99.9 %	99.8 %
Absorption correction	Semi-empirical from equivalents	Semi-empirical from equivalents	Semi-empirical from equivalents
Max,. min. transmission	0.5675, 0.4024	0.746, 0.6579	0.7465, 0.6129
Refinement method	Full-matrix least-squares on F^2	Full-matrix least-squares on F^2	Full-matrix least-squares on F^2
Data / restraints / parameters	8524 / 0 / 253	7753 / 0 / 383	23599 / 0 / 849
Goodness-of-fit	1.037	1.077	1.013
R1, wR2 [I>2sigma(I)]	0.0269, 0.0455	0.0348, 0.0533	0.0226, 0.0478

R1, wR2 (all data)	0.0354, 0.0474	0.0478, 0.0582	0.0297, 0.0498
Largest diff. peak and hole, e.Å^{-3}	0.959, -2.147	1.442, -1.378	0.850, -0.954
CCDC	2292786	2292787	2292788

TableS2. Fragmentof .prp file for the single crystal of **2_1**.

SPACE GROUP DETERMINATION

Lattice exceptions:	P	A	B	C	I	F	Obv	Rev	All
N (total) =	0	48804	49064	48886	48872	73377	65126	65148	97728
N (int>3sigma) =	0	38960	34978	39280	39183	56609	52235	52138	78149
Mean intensity =	0.0	32.5	11.4	32.4	32.7	25.4	32.8	32.6	32.6
Mean int/sigma =	0.0	15.0	10.2	15.0	15.0	13.4	15.0	15.0	15.0

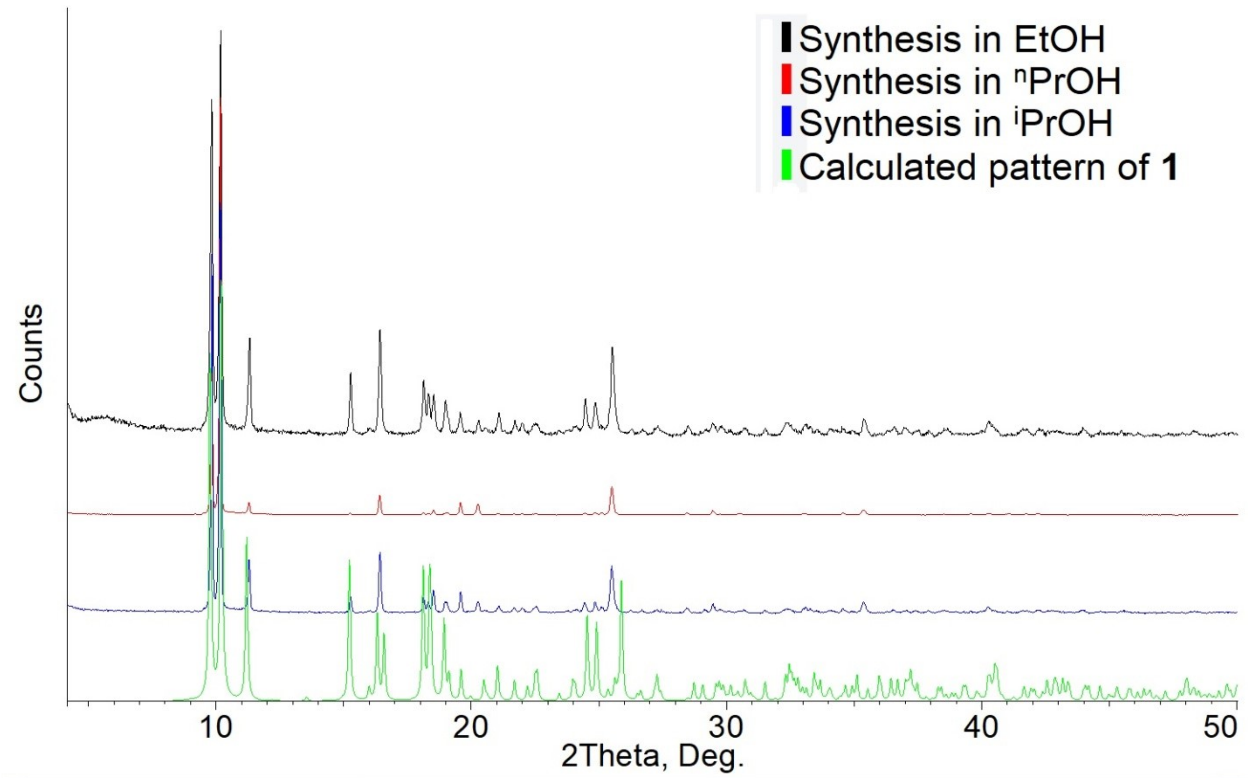

Fig. S1. Powder XRD patterns of products of syntheses of **1** in various alcohols compared to the calculated pattern of **1** structure.

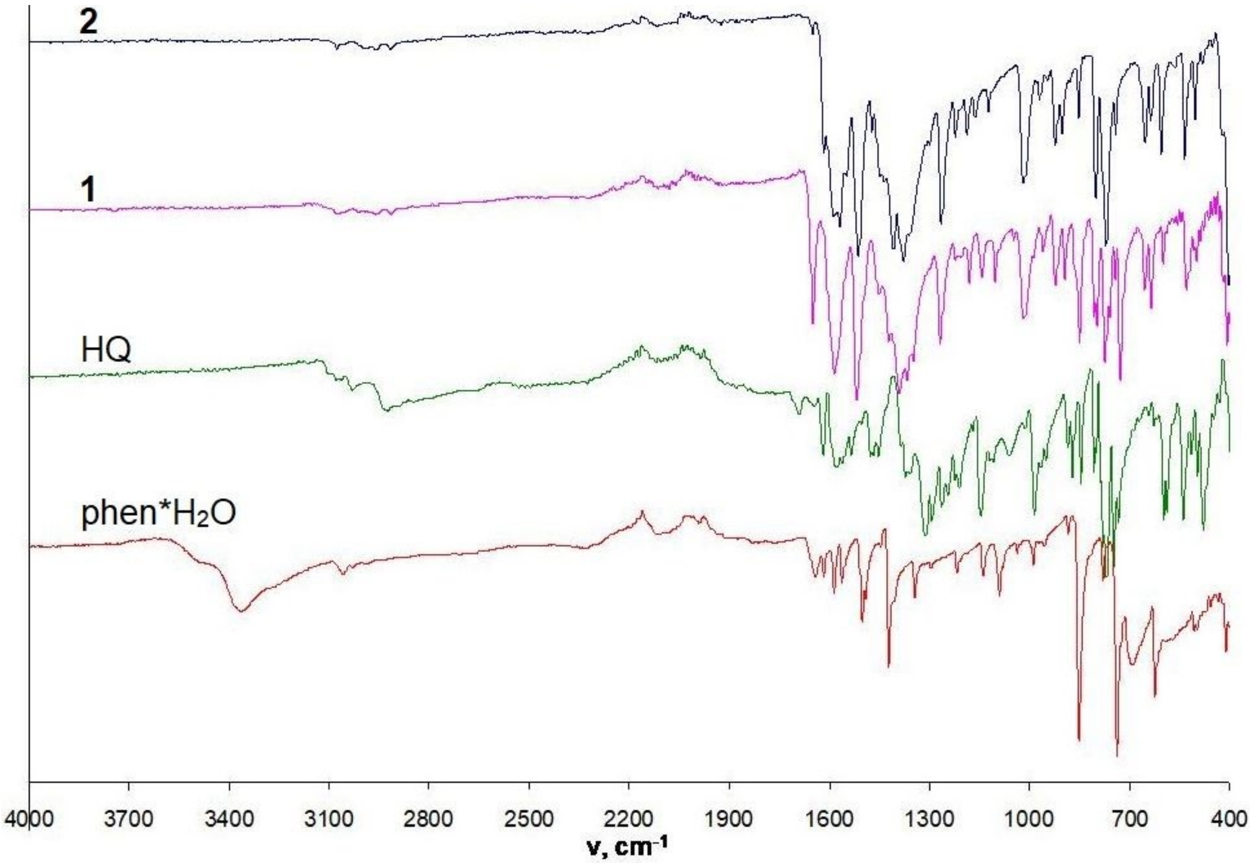

Fig. S2. IR spectra of complexes **1** and **2** compared with those of HQ and Phen·H_2O.

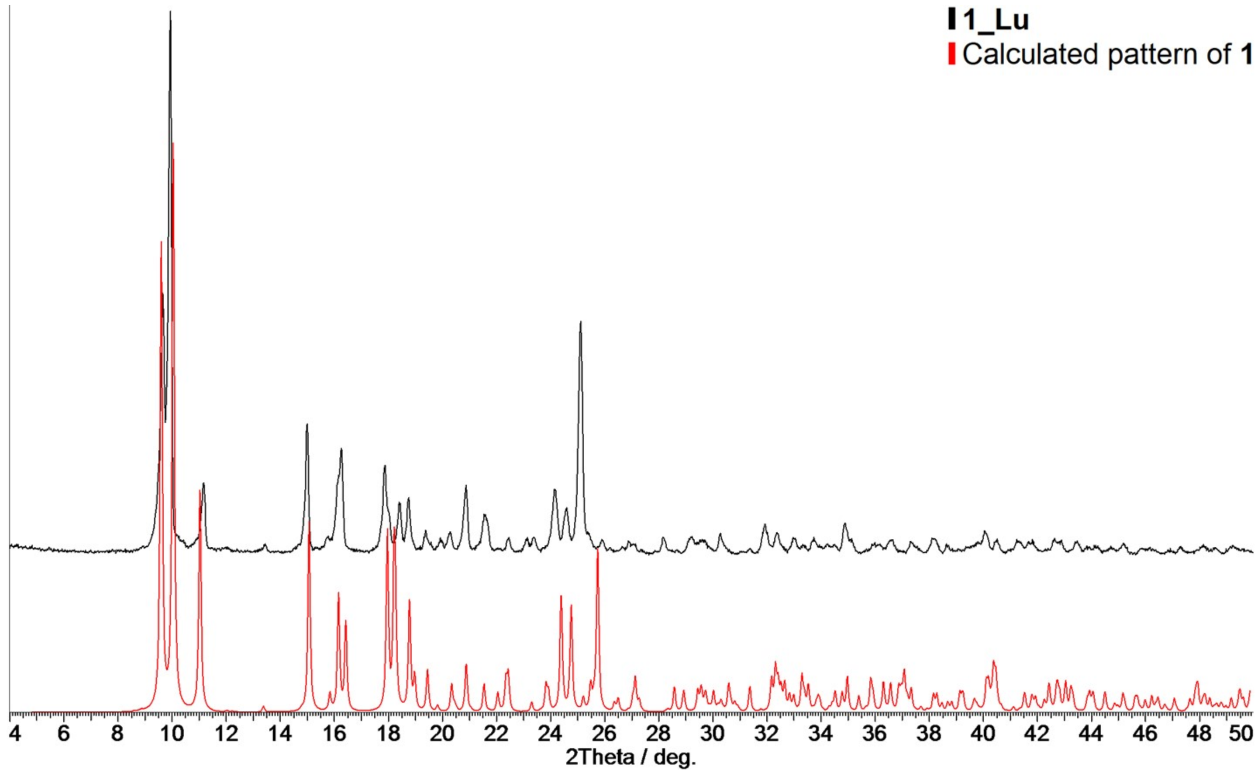

Fig. S3. Powder XRD pattern of the product of the synthesis of **1_Lu** compared to calculated pattern of **1** structure.

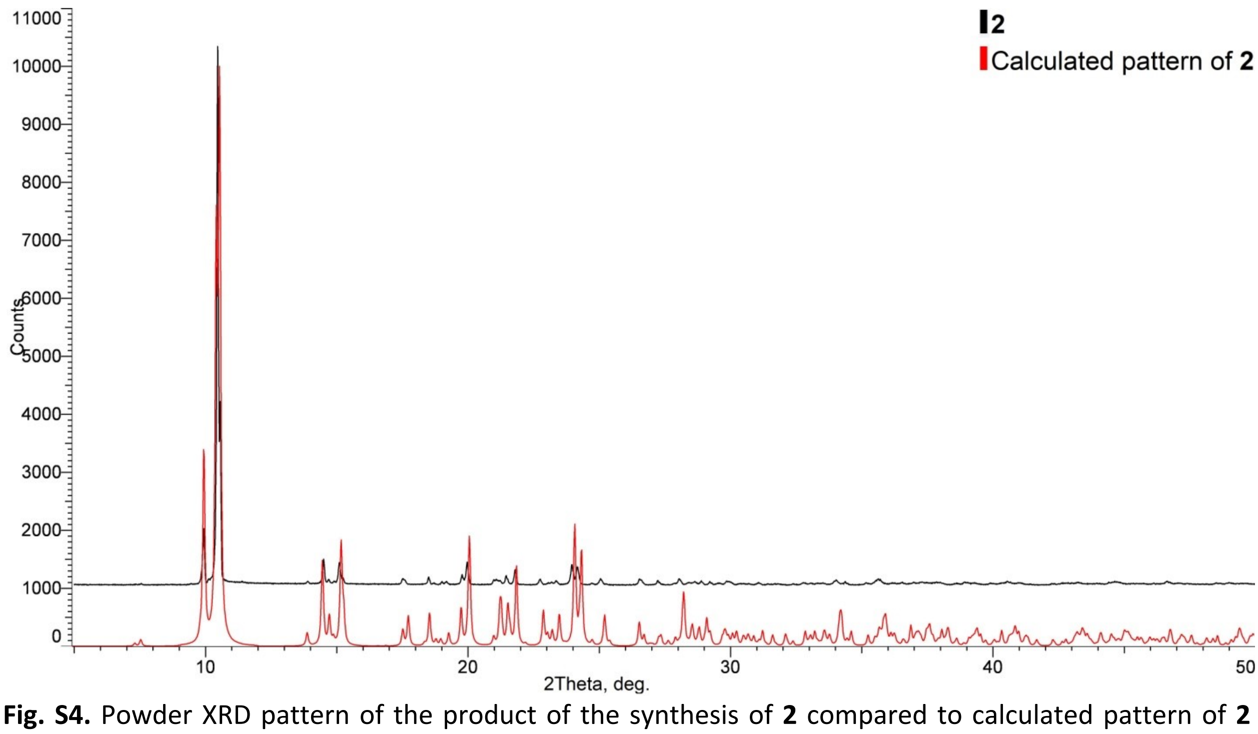

Fig. S4. Powder XRD pattern of the product of the synthesis of **2** compared to calculated pattern of **2** structure.

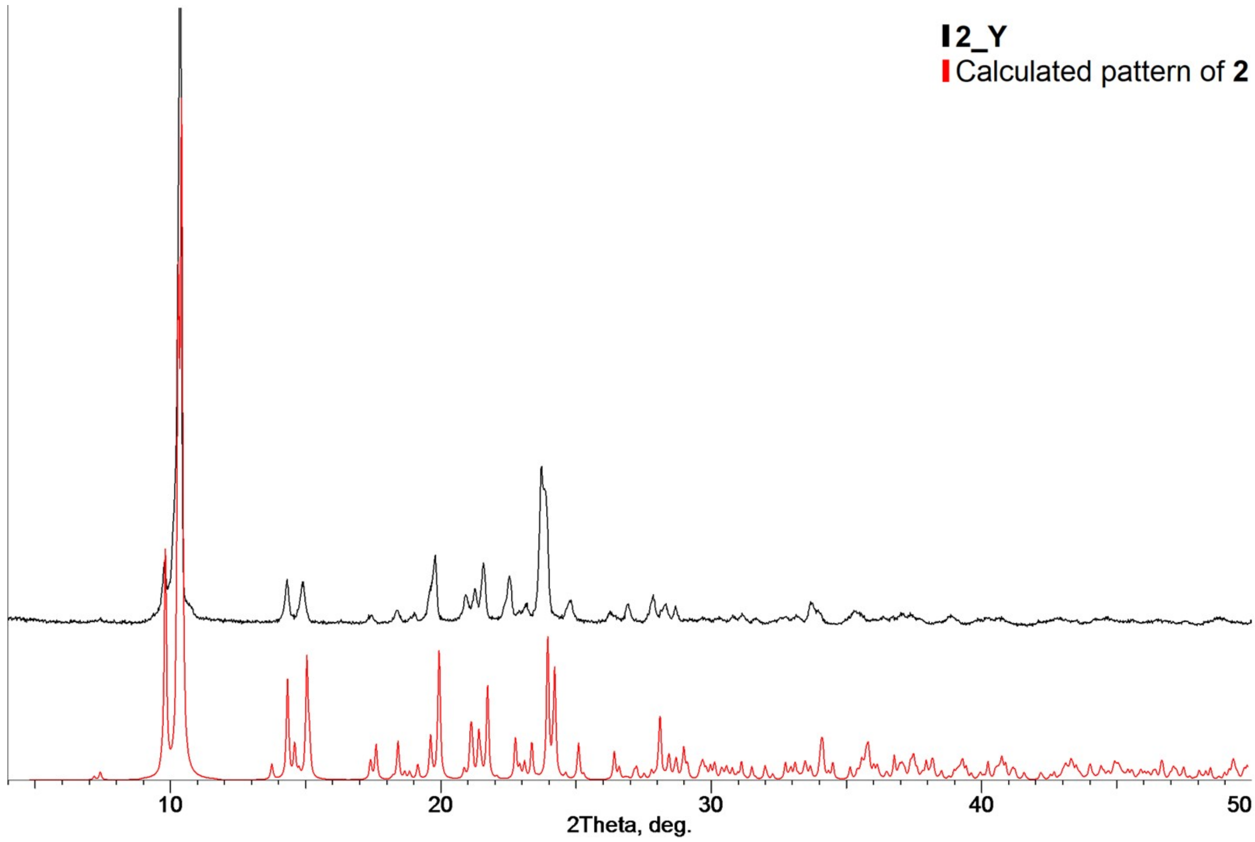

Fig. S5. Powder XRD pattern of the product of the synthesis of **2_Y** compared to calculated pattern of **2** structure.

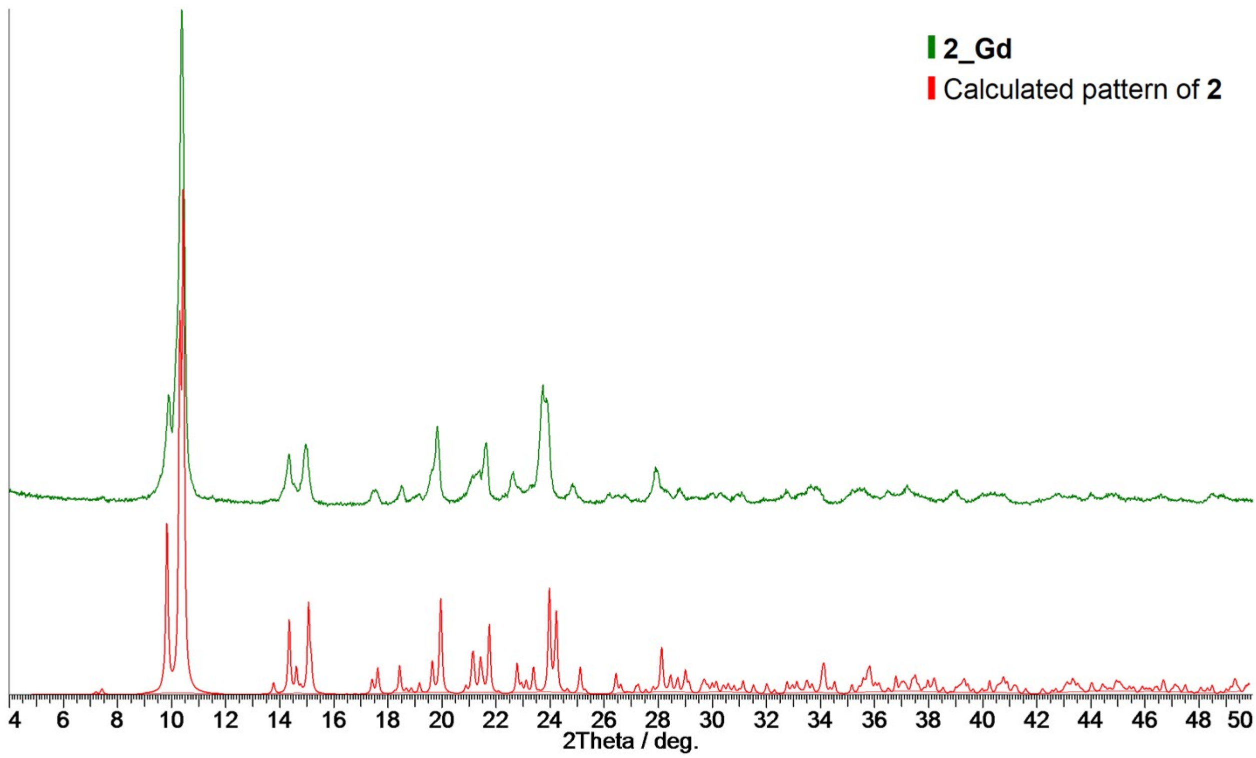

Fig. S6. Powder XRD pattern of the product of the synthesis of **2_Gd** compared to calculated pattern of **2** structure.

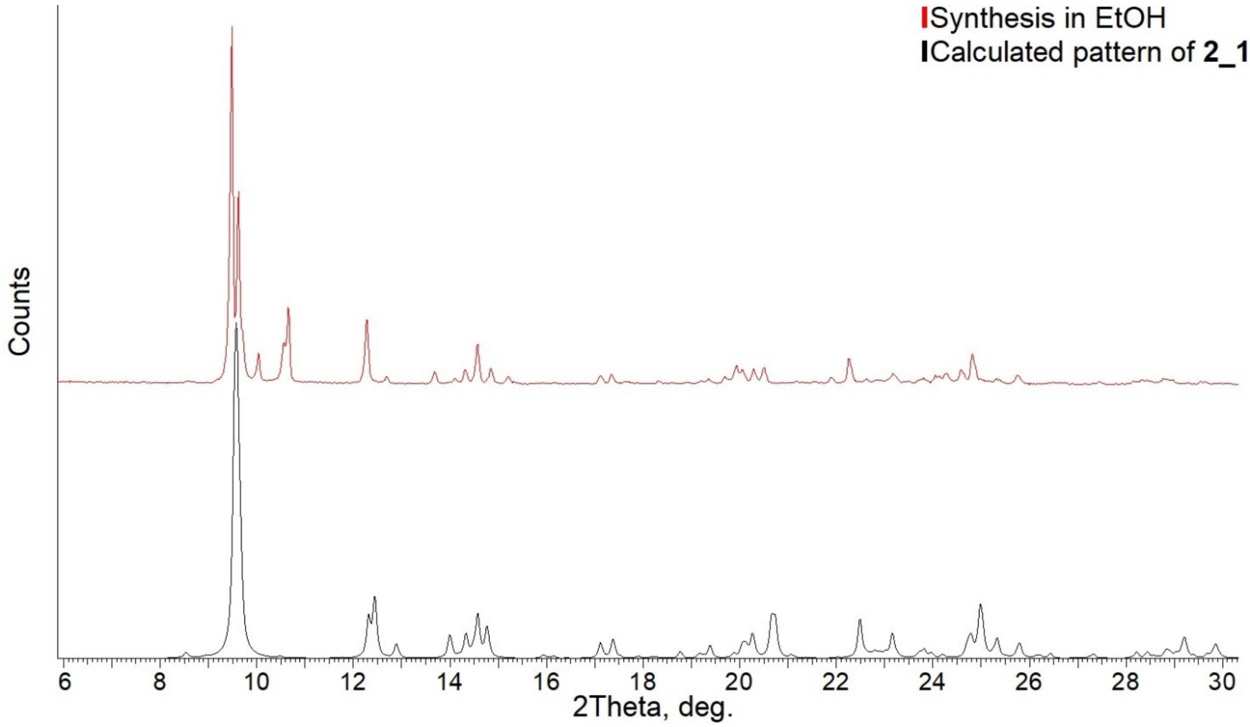

Fig. S7. Powder XRD pattern of the product of the synthesis of **2_1** from EtOH compared to calculated pattern of **2_1** structure.

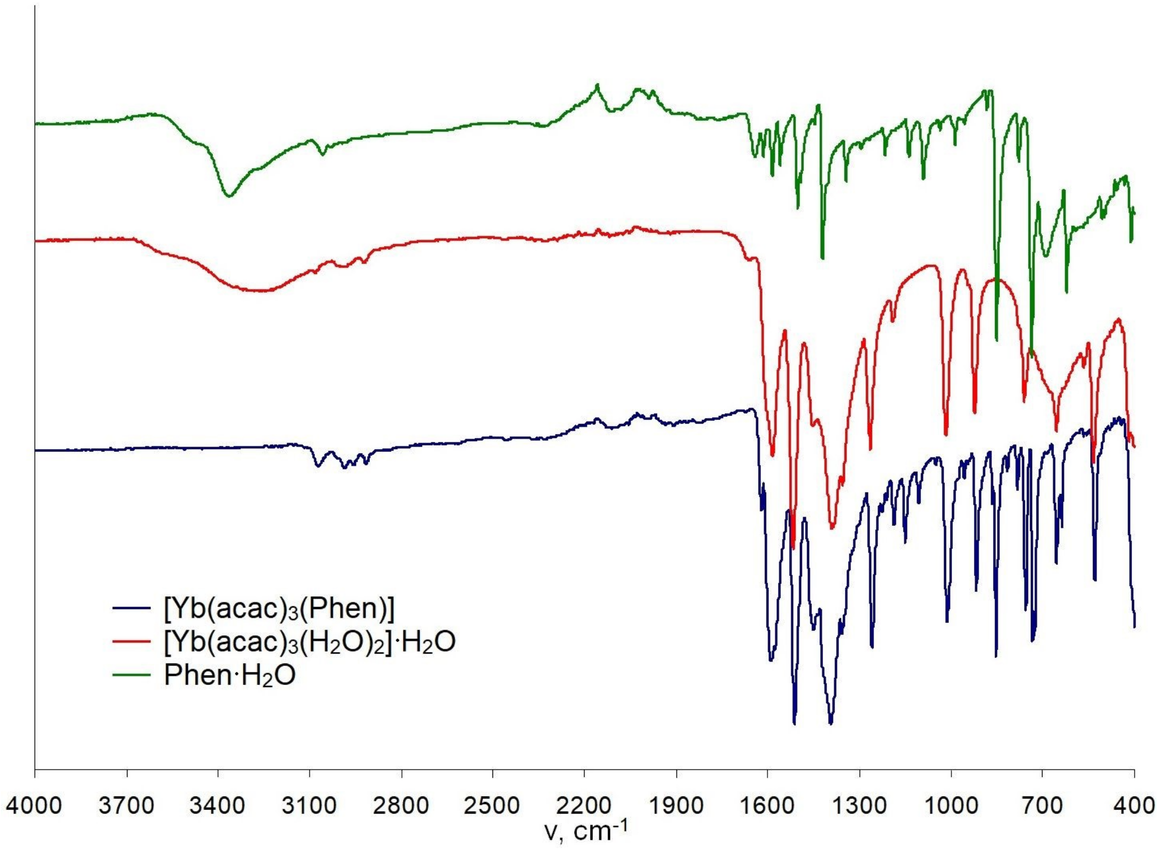

Fig. S8. IR spectrum of the intermediate product precipitated during the alternative synthesis of **2** (blue line, see *p. 3.1.* of the main text) compared with the spectra of Yb(acac)$_3$·3H_2O (red line) and Phen·H_2O (green line).

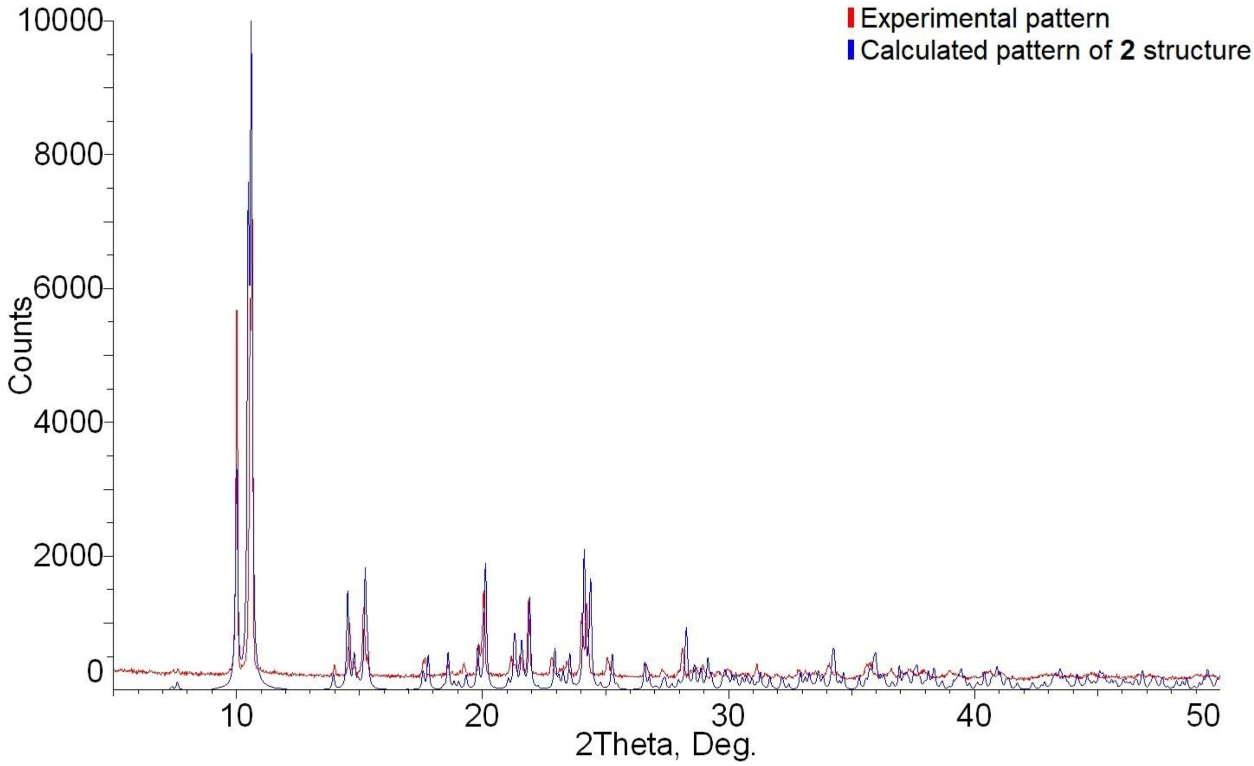

Fig. S9. Powder XRD pattern of the product isolated from the alternative synthesis of **2**(see *p. 3.1.* of the main text) compared to calculated pattern of **2**structure.

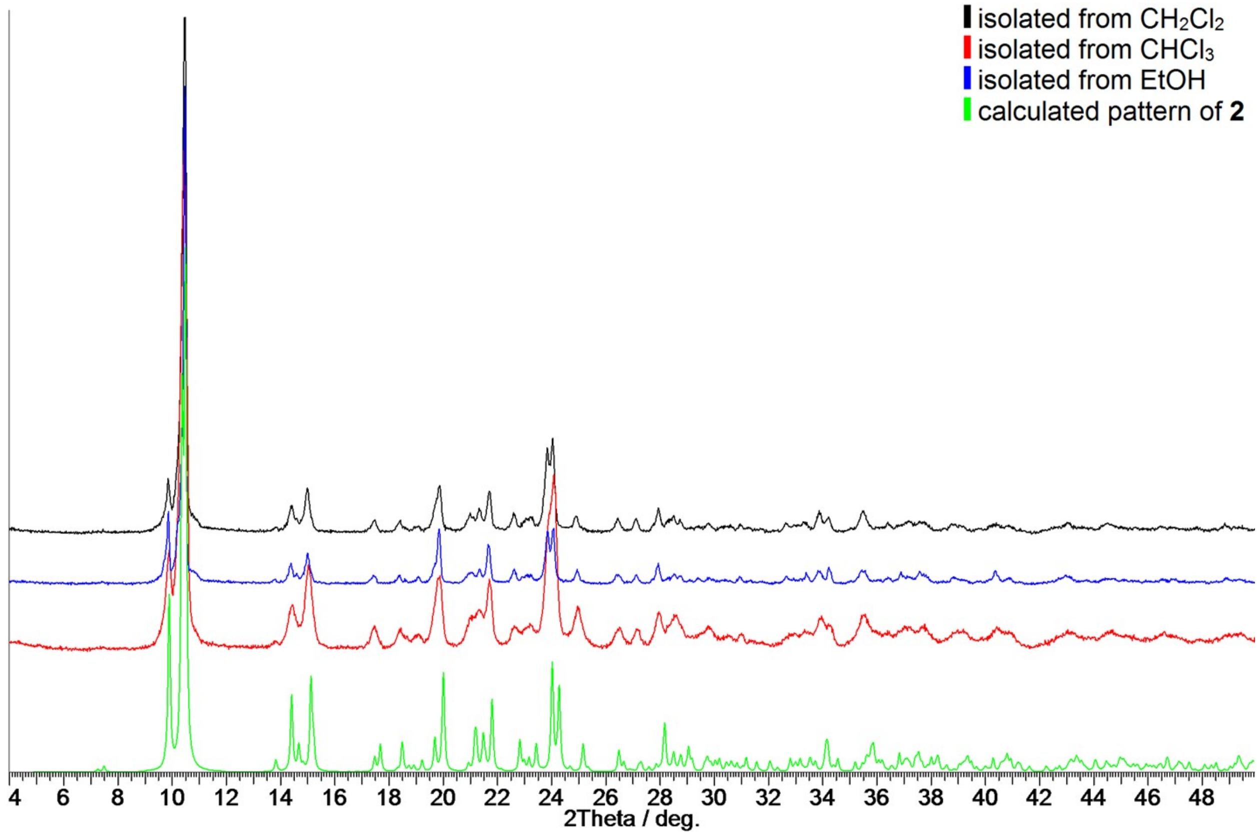

Fig. S10. Powder XRD patterns of the products isolated from the solutions of **2** in CH_2Cl_2, $CHCl_3$and EtOH compared to calculated pattern of **2** structure.

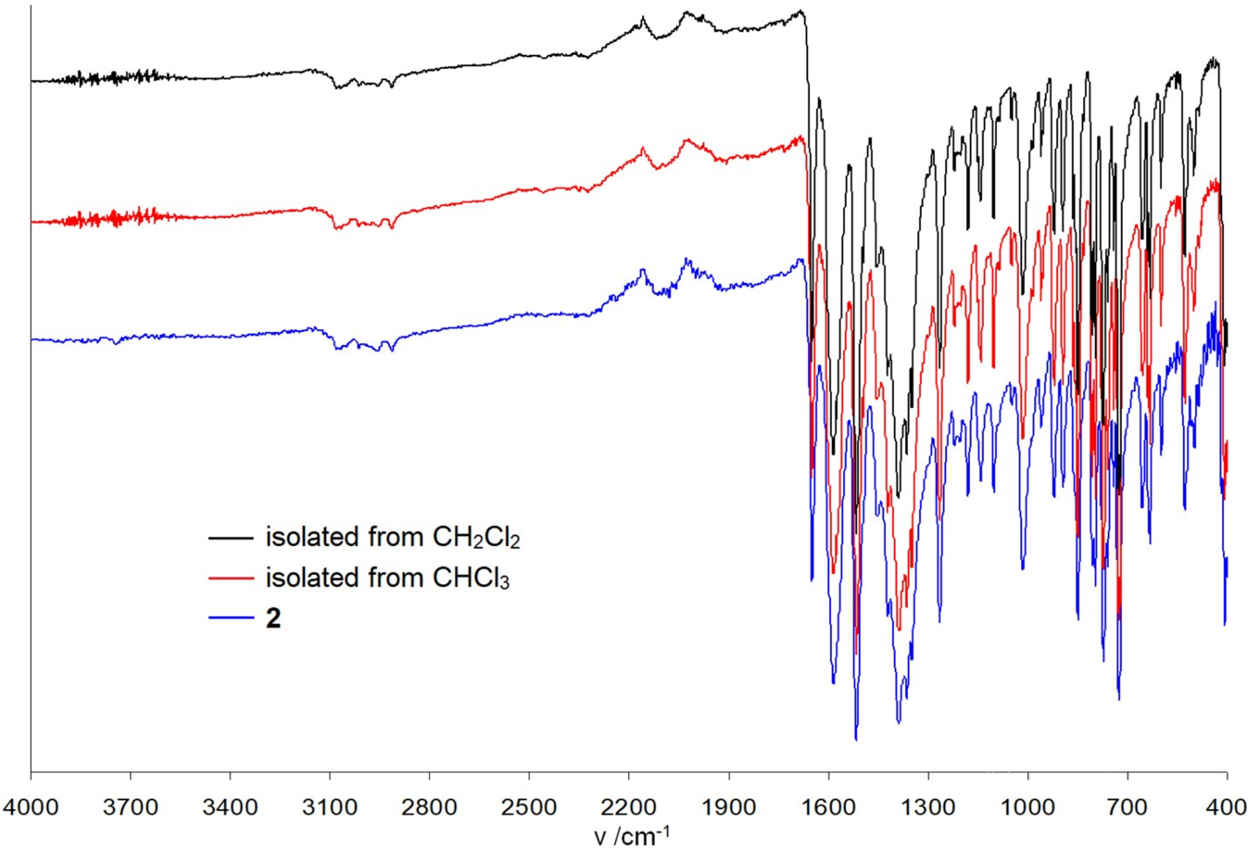

Fig. S11. IR spectra of the products isolated from the solutions of **2** in CH_2Cl_2 and $CHCl_3$.

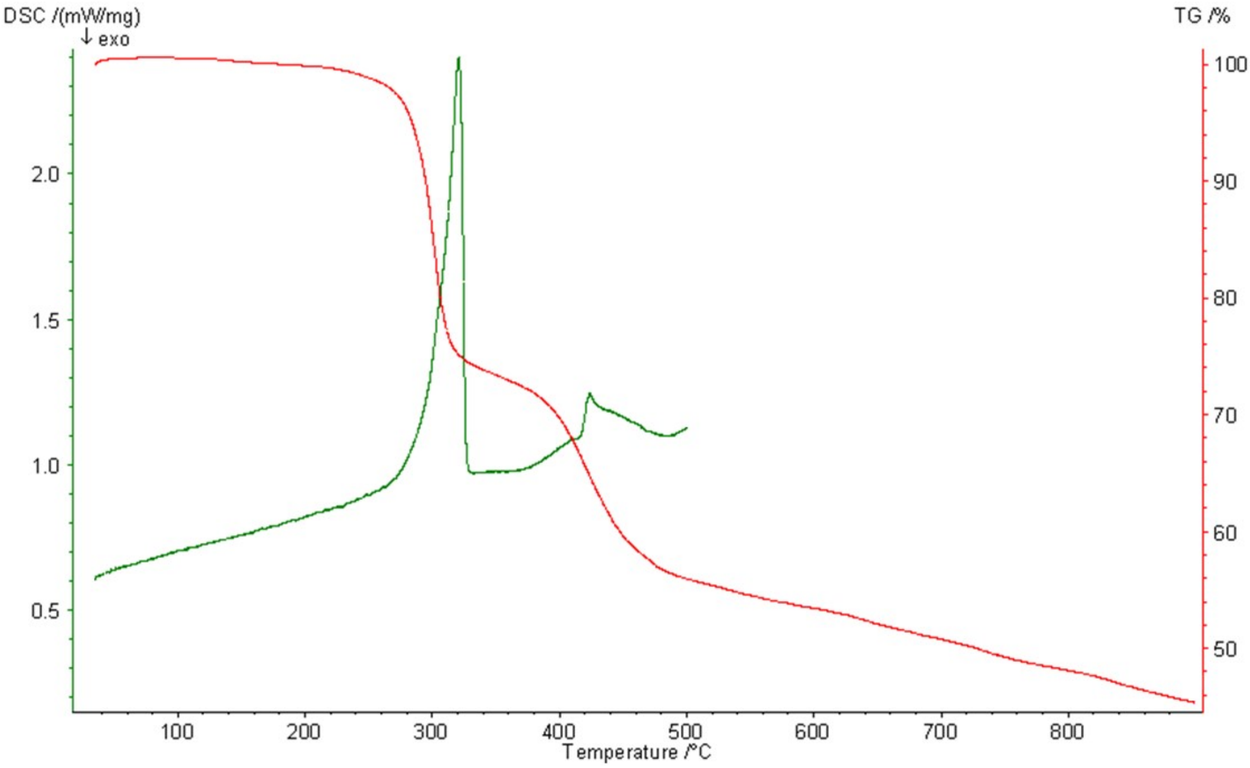

Fig. S12. TG (red) and DSC (green) curves of complex **1** on heating under Ar flow.

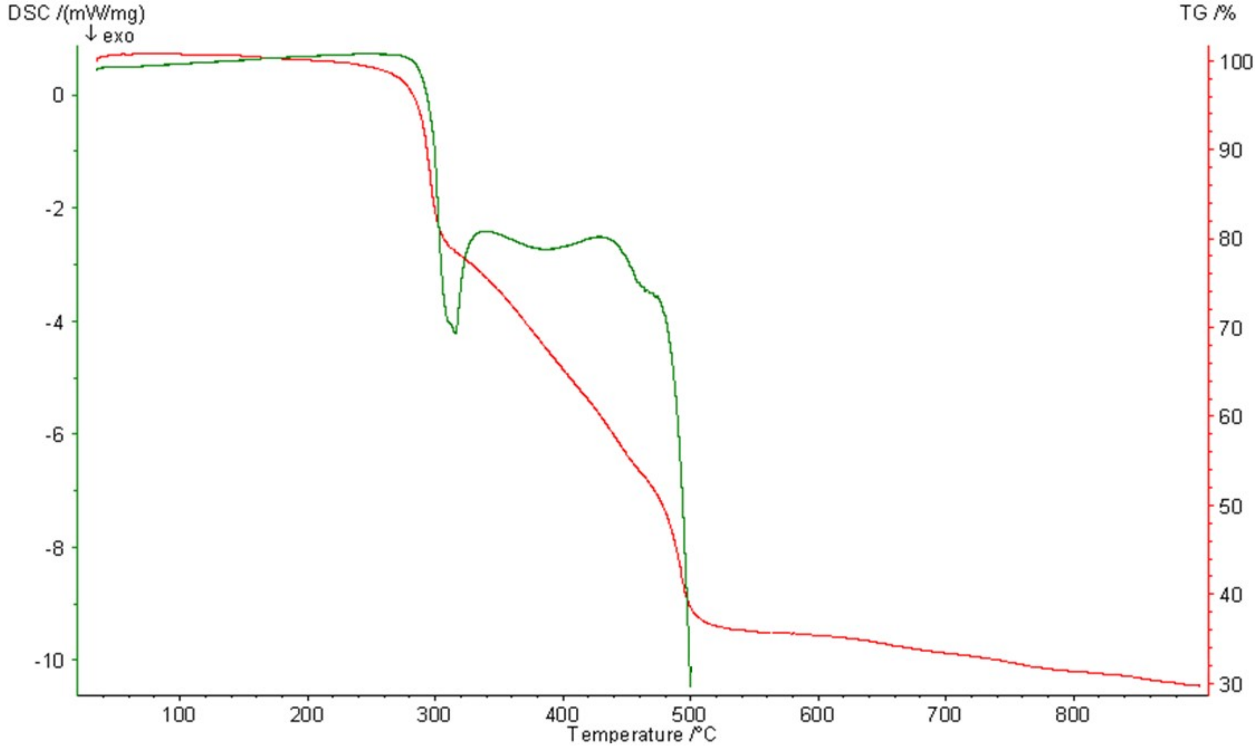

Fig. S13. TG (red) and DSC (green) curves of complex **1** on heating under artificial air flow.

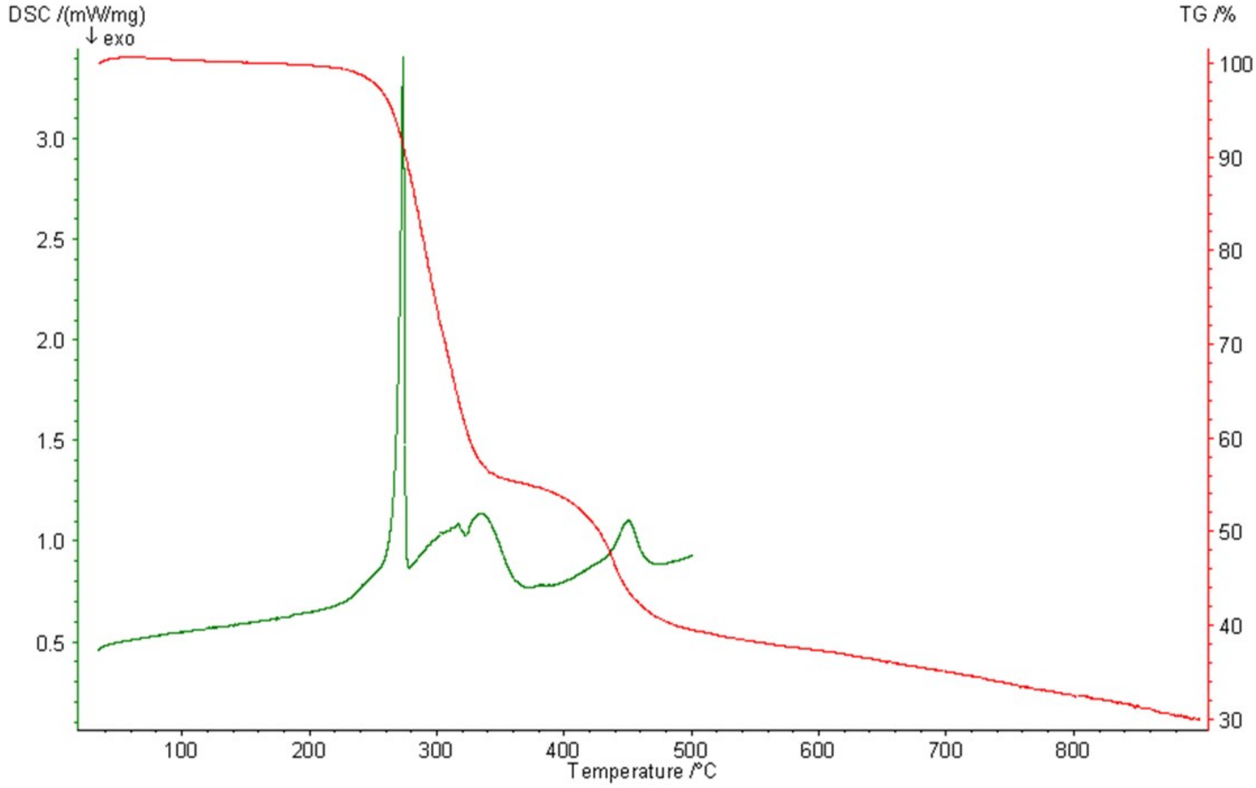

Fig. S14. TG (red) and DSC (green) curves of complex **2** on heating under Ar flow.

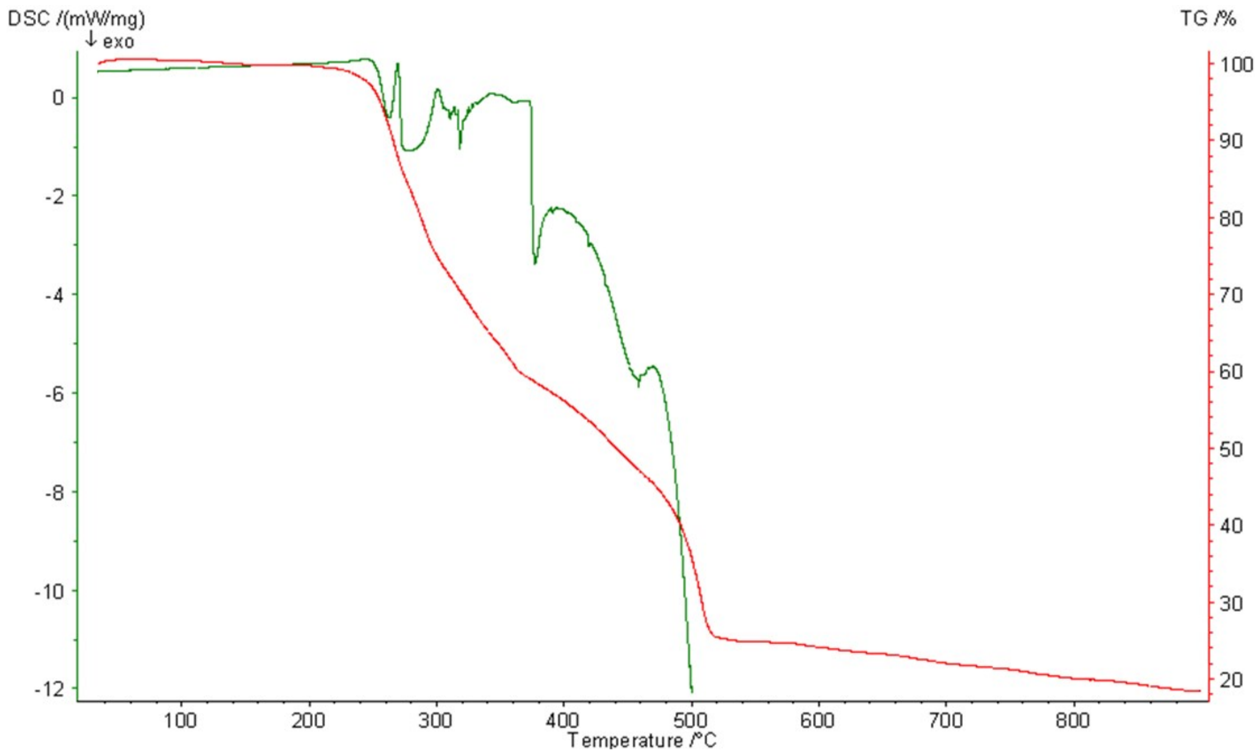

Fig. S15. TG (red) and DSC (green) curves of complex **2** on heating under artificial air flow.

TableS3. Shortest C…C contacts (Å) in stacking interactions within **1**, **2** and **2_1** structures.

1	
C(2)…C(6) (-x, -y+1, -z)	3.346
C(4)…C(4) (-x, -y+1, -z)	3.359
2	
C(1)…C(5) (-x, -y, -z+1)	3.331
C(2)…C(6) (-x, -y, -z+1)	3.492
C(3)…C(9) (-x, -y, -z+1)	3.407
C(4)…C(4) (-x, -y, -z+1)	3.496
C(22)…C(26) (-x+1, -y+1, -z)	3.311
C(24)…C(24) (-x+1, -y+1, -z)	3.395
2_1	
C(1)…C(35)	3.438
C(3)…C(33)	3.514
C(5)…C(42)	3.484
C(10)…C(37)	3.487
C(22)…C(28) (-x, -y, -z+1)	3.421
C(23)…C(27) (-x, -y, -z+1)	3.385
C(23)…C(28) (-x, -y, -z+1)	3.410
C(25)…C(32) (-x, -y, -z+1)	3.478
C(55)…C(59) (-x+3, -y+2, -z+2)	3.479
C(55)…C(60) (-x+3, -y+2, -z+2)	3.341
C(56)…C(59) (-x+3, -y+2, -z+2)	3.475
C(58)…C(64) (-x+3, -y+2, -z+2)	3.500

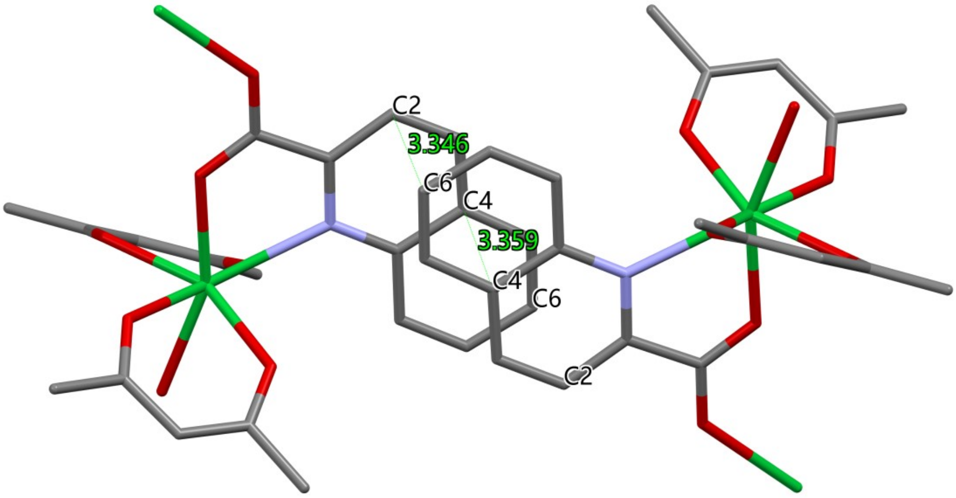

Fig.S16. Stacking interactions in the structure **1**.

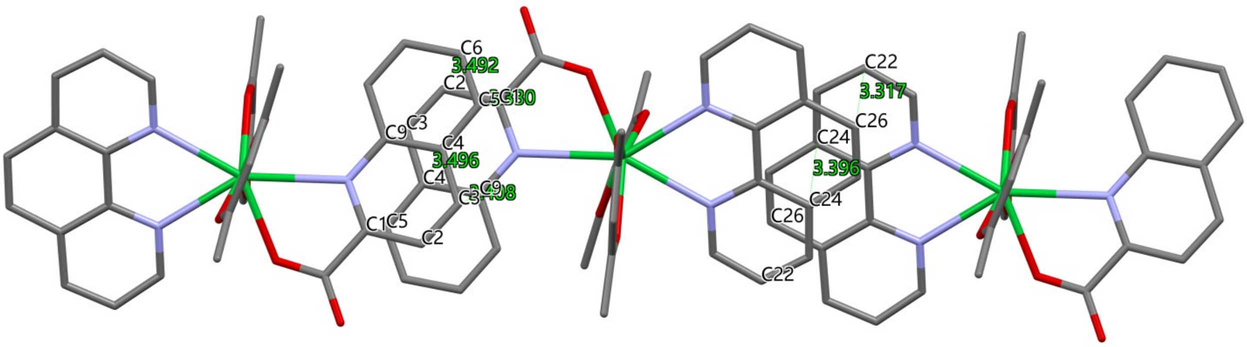

Fig.S17. Stacking interactions in the structure **2**.

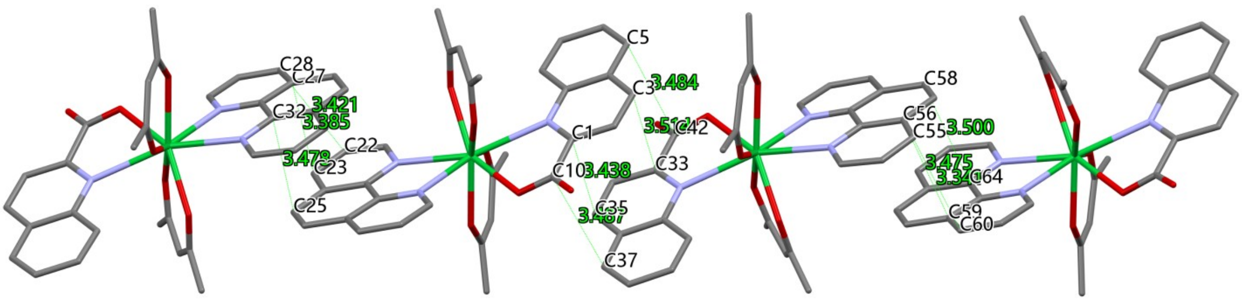

Fig.S18. Stacking interactions in the structure **2_1**.

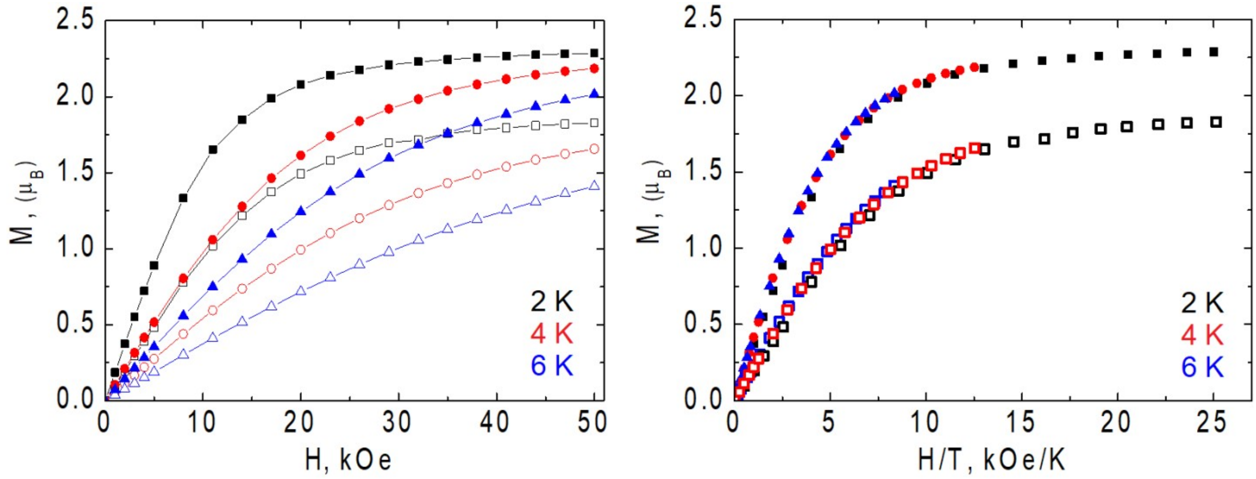

Fig. S19. Low-temperature magnetization *vs.* H (left) and *vs.* HT^{-1} (right) for complex **1** (per one Yb^{3+} ion, empty simbols) and **2** (filled simbols).

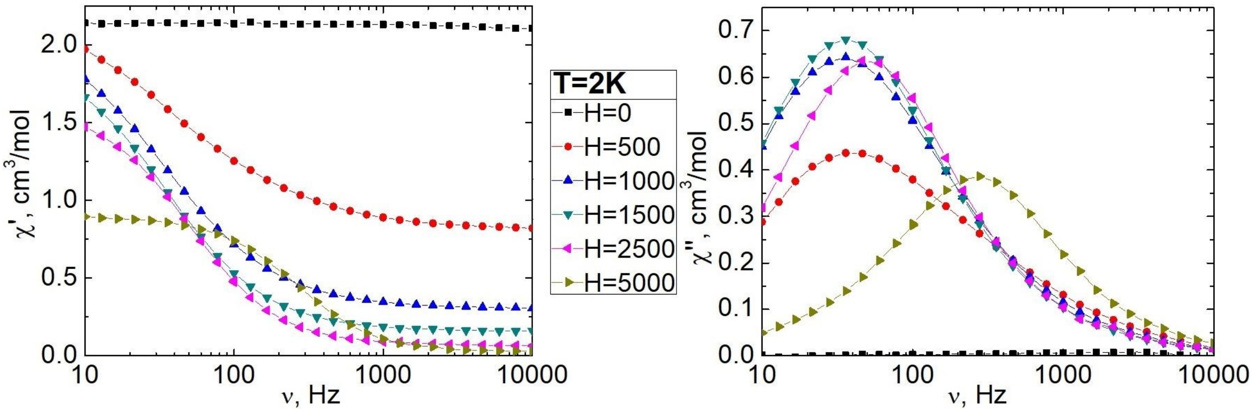

Fig. S20. Frequency dependencies of the in-phase (χ') and out-of-phase (χ'') components of the dynamic magnetic susceptibility of **1** at varied strength of the external static magnetic field and T=2K. Solid lines are visual guides.

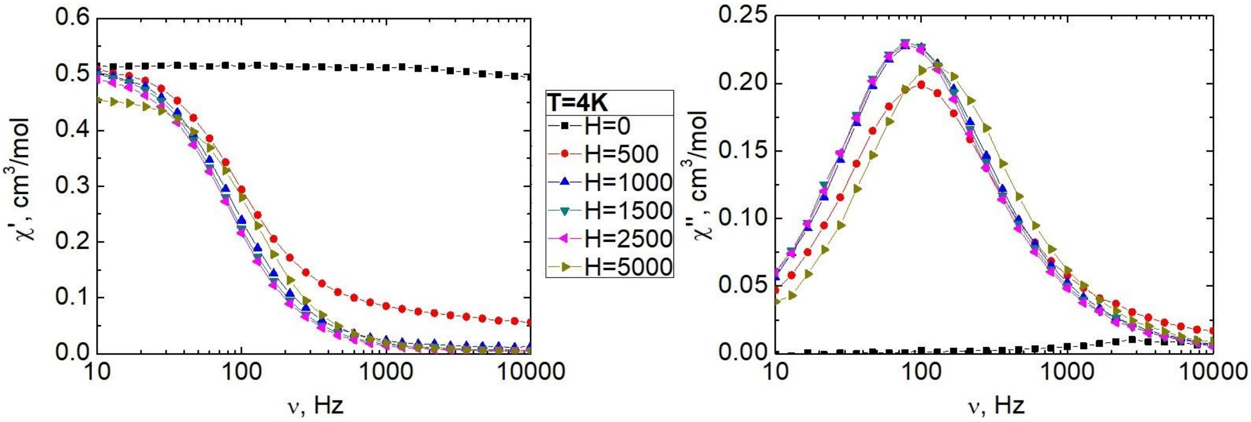

Fig. S21. Frequency dependencies of the in-phase (χ') and out-of-phase (χ'') components of the dynamic magnetic susceptibility of **2** at varied strength of the external static magnetic field andT=4K. Solid lines are visual guides.

Table S4. Fitting of the τ *vs.* T dependences for **1** (H_{DC} = 1.5 kOe, T = 2-7 K).

<table>
<tr><th>Fitting</th><th>Fit function, temperature range, and the best-fit parameters with uncertainties</th></tr>
<tr><td>
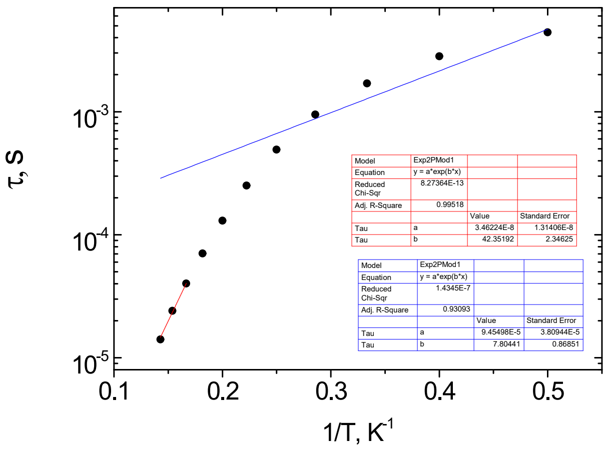

</td><td>
Orbach
$\tau = \tau_0 \cdot \exp(\Delta E/kT)$

T = 6-7 K
$\Delta E/k$ = 42 ± 2 K
$\tau_0 = 3 \cdot 10^{-8} \pm 1 \cdot 10^{-8}$s
R^2 = 0.99518(red line)

T = 2-7 K
$\Delta E/k$ =7.8 ±0.9 K
$\tau_0 = 9 \cdot 10^{-5} \pm 4 \cdot 10^{-5}$ s
R^2 = 0.93093(blue line)
</td></tr>
<tr><td>
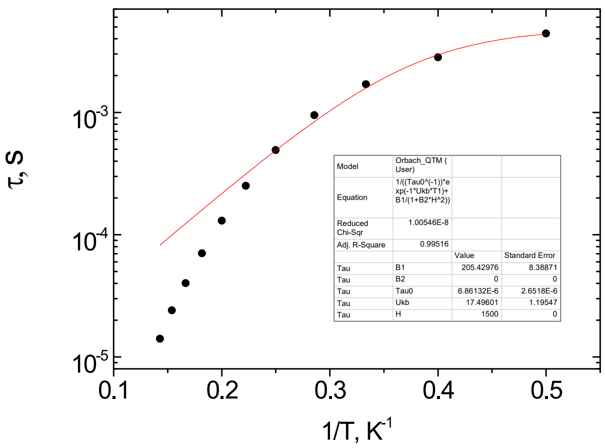

</td><td>
Orbach+QTM
$\tau^{-1} = \tau_0^{-1} \cdot \exp(-\Delta E/kT)$+B

$\Delta E/k$ = 17±1 K
$\tau_0 = 7 \cdot 10^{-6} \pm 3 \cdot 10^{-6}$ s
B= 205 ± 8 s^{-1}
R^2 = 0.99516
</td></tr>
<tr><td>
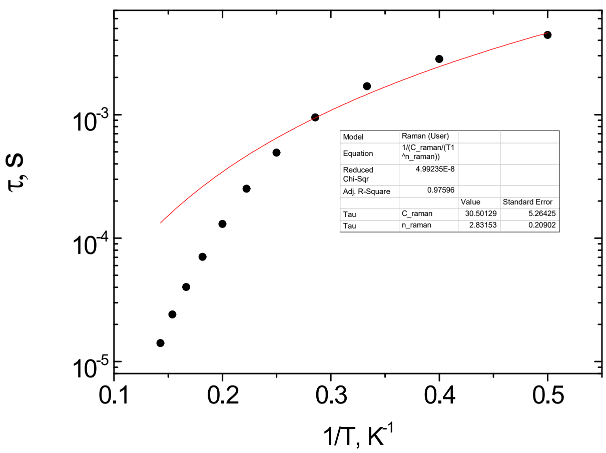

</td><td>
Raman
$\tau^{-1} = C_{Raman} T^{n\_Raman}$

C_{Raman}=31± 5$s^{-1}K^{-nRaman}$
n_{Raman}=2.8±0.2
R^2 = 0.97596
</td></tr>
</table>

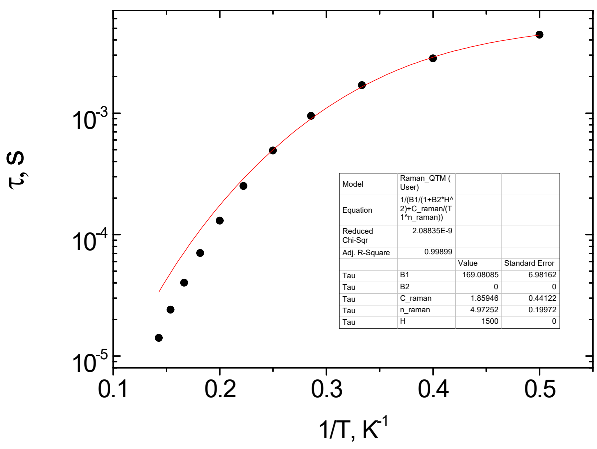

Raman+ QTM

$\tau^{-1} = C_{Raman}T^{nRaman} + B$

C_{Raman}= 1.9± 0.4 $s^{-1}K^{-nRaman}$

n_{Raman}= 5.0± 0.2

B = 169± 7 s^{-1}

R^2 = 0.99899

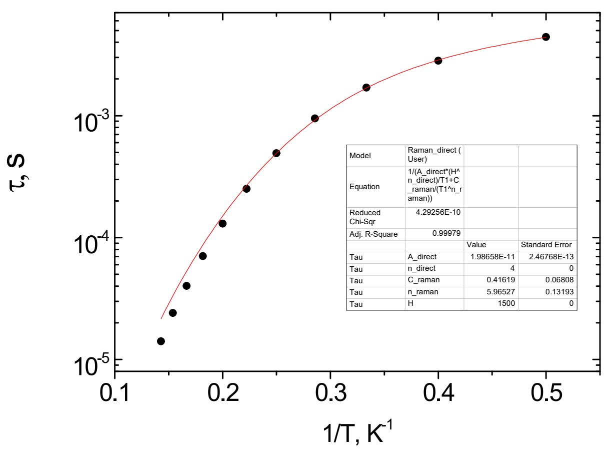

Raman+Direct

$\tau^{-1} = C_{Raman}T^{nRaman} + A_{direct}TH^4$

C_{Raman}= 0.42± 0.07 $s^{-1}K^{-nRaman}$

n_{Raman}=6.0± 0.1

A_{direct} = $1.99\cdot10^{-11} \pm 2\cdot10^{-13}$ $K^{-1}Oe^{-4}s^{-1}$

R^2 = 0.99979

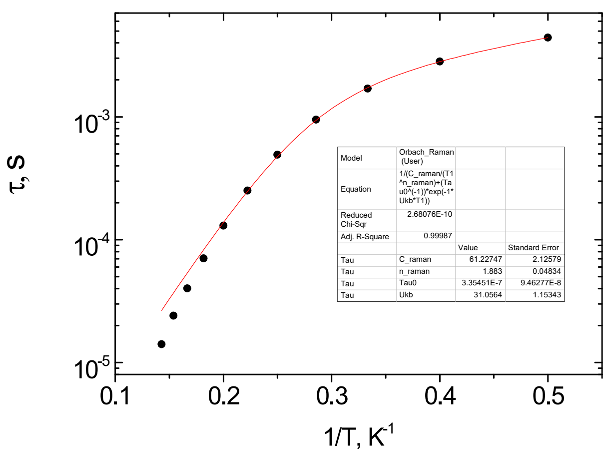

Orbach+Raman

$\tau^{-1} = \tau_0^{-1}\cdot\exp(-\Delta E/kT)+C_{Raman}T^{nRaman}$

$\Delta E/k$ = 31± 1 K

τ_0=$3.4\cdot10^{-7} \pm 9\cdot10^{-8}$ s

C_{Raman}= 61± 2 $s^{-1}K^{-nRaman}$

n_{Raman}= 1.88± 0.05

R^2 = 0.99987

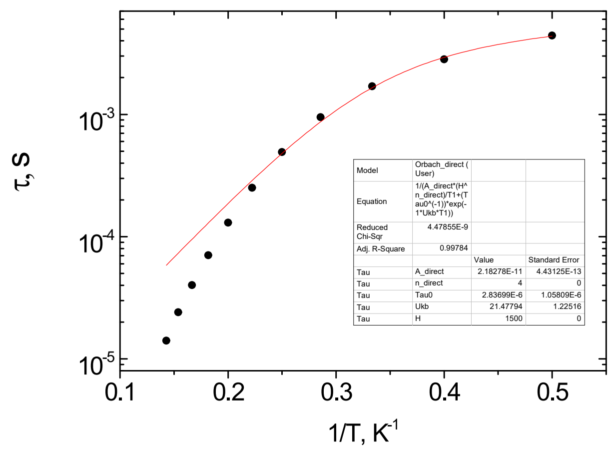

Orbach+Direct

$\tau^{-1} = \tau_0^{-1}\cdot\exp(-\Delta E/kT)+A_{direct}TH^4$

$\Delta E/k$ = 21± 1 K

τ_0= $3\cdot10^{-6} \pm 1\cdot10^{-6}$s

A_{direct} = $2.18\cdot10^{-11} \pm 4\cdot10^{-13}$ $K^{-1}Oe^{-4}s^{-1}$

R^2 = 0.99784

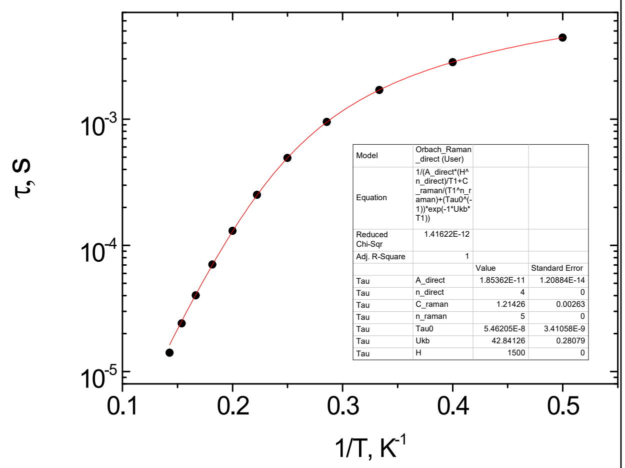

Orbach+Raman+Direct

$\tau^{-1} = \tau_0^{-1}\cdot\exp(-\Delta E/kT)+C_{Raman}T^{nRaman}+A_{direct}TH^4$

$\Delta E/k$ = 42.8±0.3 K

τ_0= $5.5\cdot10^{-8} \pm 3\cdot10^{-9}$ s

C_{Raman}= 1.214±0.003 $s^{-1}K^{-nRaman}$

n_{Raman}= 5 (fixed)

A_{direct} = $1.854\cdot10^{-11} \pm 1\cdot10^{-14}$ $K^{-1}Oe^{-4}s^{-1}$

R^2 = 1

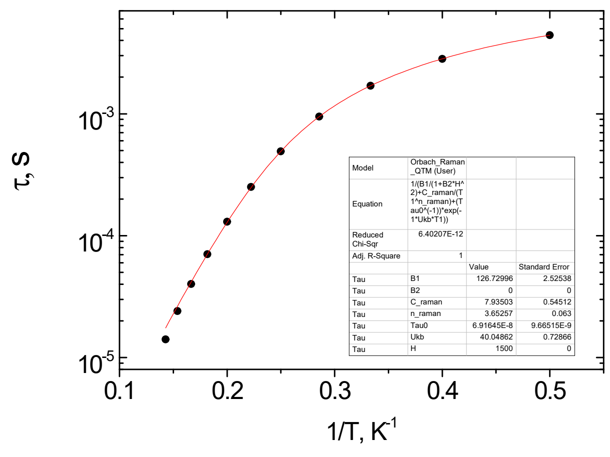

Orbach+Raman+QTM

$\tau^{-1} = \tau_0^{-1}\cdot\exp(-\Delta E/kT)+C_{Raman}T^{nRaman}+B$

$\Delta E/k$ = 40.0±0.7 K

τ_0=$7\cdot10^{-8} \pm 1\cdot10^{-8}$ s

C_{Raman}=7.9±0.5 $s^{-1}K^{-nRaman}$

n_{Raman}= 3.65± 0.06

B = 127±3s^{-1}

R^2 = 1

Table S5. Fitting ofthe τ *vs.T* dependences for**2** (H = 1.5 kOe, T = 2.5-8.5 K).

<table>
<tr><th>Fitting</th><th>Fit function, temperature range, and the best-fit parameters with uncertainties</th></tr>
<tr><td>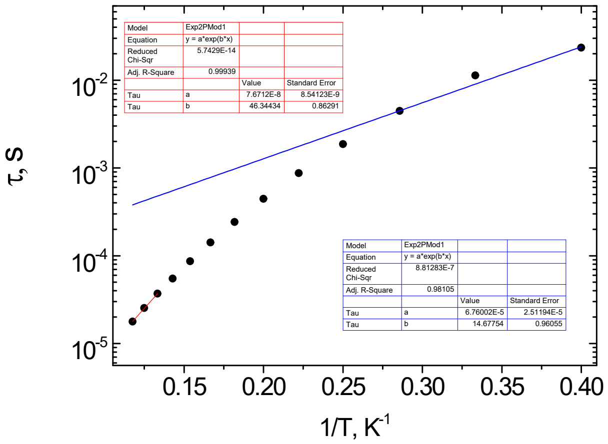
</td>
<td>Orbach
$\tau = \tau_0 \cdot \exp(\Delta E/kT)$

T = 7.5-8.5 K
$\Delta E/k$ = 46.3 ±0.9 K
τ_0= $7.7 \cdot 10^{-8} \pm 9 \cdot 10^{-9}$ s
R^2 = 0.99939(red line)

T = 2.5-8.5 K
$\Delta E/k$ = 15 ± 1 K
τ_0= $7 \cdot 10^{-5} \pm 3 \cdot 10^{-5}$ s
R^2 = 0.98105(blue line)</td></tr>
<tr><td>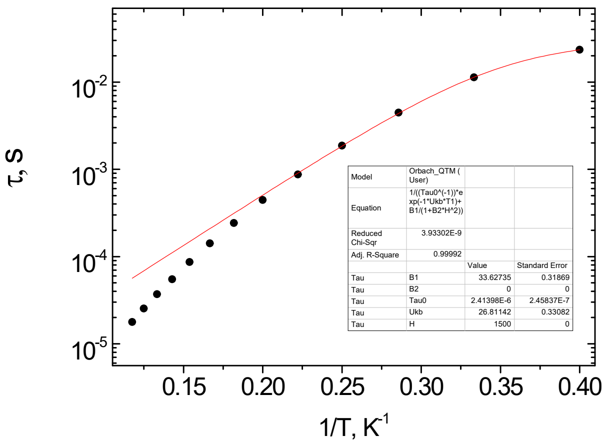
</td>
<td>Orbach+QTM
$\tau^{-1} = \tau_0^{-1} \cdot \exp(-\Delta E/kT)$+B

$\Delta E/k$ = 26.8±0.3 K
τ_0= $2.4 \cdot 10^{-6} \pm 2 \cdot 10^{-7}$ s
B= 33.6±0.3s^{-1}
R^2 = 0.99992</td></tr>
<tr><td>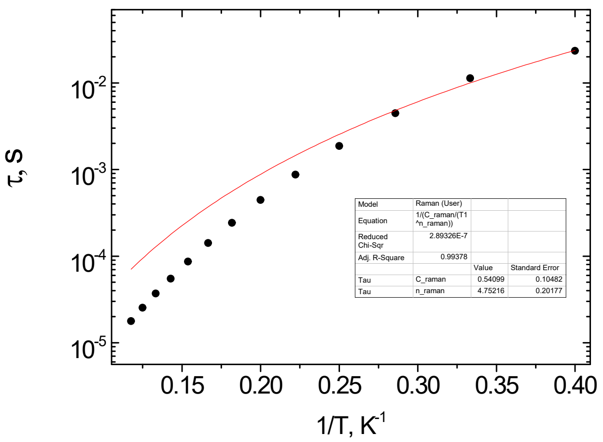
</td>
<td>Raman
$\tau^{-1} = C_{Raman} T^{n\_Raman}$

C_{Raman}= 0.5± 0.1 $s^{-1}K^{-nRaman}$
n_{Raman}=4.8 ± 0.2
R^2 = 0.99378</td></tr>
</table>

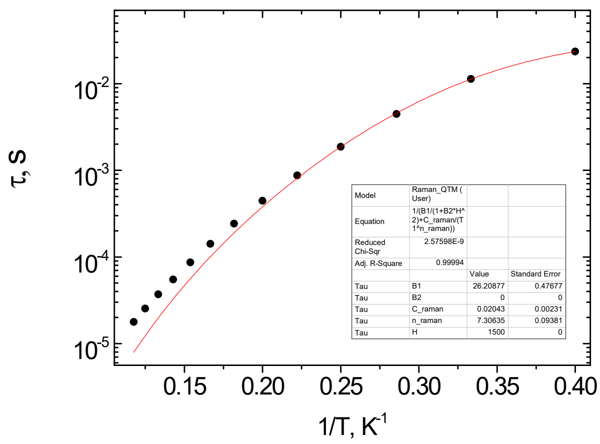

Raman+ QTM

$\tau^{-1} = C_{Raman}T^{nRaman} + B$

C_{Raman}= 0.020± 0.002 $s^{-1}K^{-nRaman}$

n_{Raman}= 7.31±0.09

B = 26.2±0.5 s^{-1}

R^2 = 0.99994

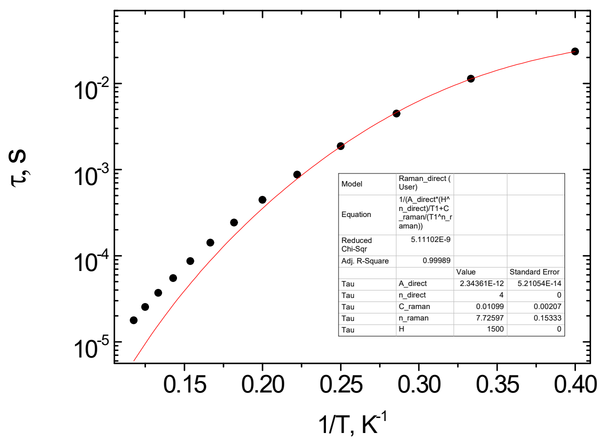

Raman+Direct

$\tau^{-1} = C_{Raman}T^{nRaman} + A_{direct}TH^4$

C_{Raman}= 0.011± 0.002 $s^{-1}K^{-nRaman}$

n_{Raman}= 7.7± 0.2

A_{direct} = $2.34\cdot10^{-12} \pm 5\cdot10^{-14}$ $K^{-1}Oe^{-4}s^{-1}$

R^2 = 0.99989

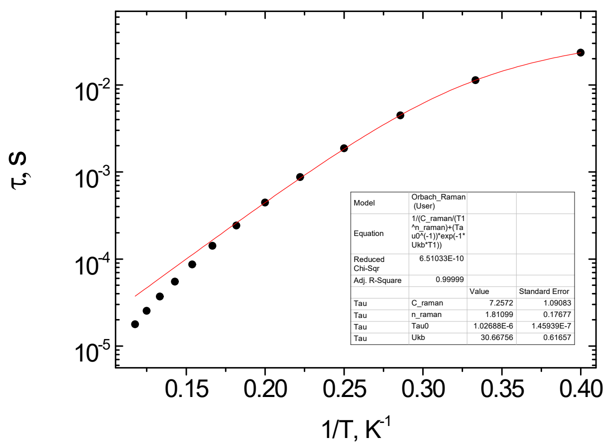

Orbach+Raman

$\tau^{-1} = \tau_0^{-1}\cdot\exp(-\Delta E/kT) + C_{Raman}T^{nRaman}$

$\Delta E/k$ = 30.7± 0.6 K

τ_0=$1.0\cdot10^{-6} \pm 1\cdot10^{-7}$ s

C_{Raman}= 7± 1 $s^{-1}K^{-nRaman}$

n_{Raman}= 1.8± 0.2

R^2 = 0.99999

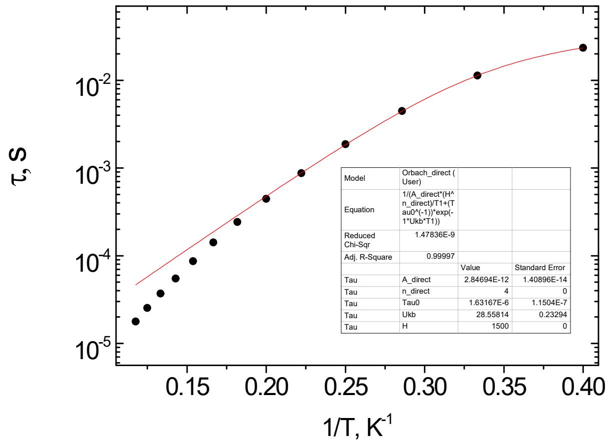

Orbach+Direct

$\tau^{-1} = \tau_0^{-1} \cdot \exp(-\Delta E/kT) + A_{direct} T H^4$

$\Delta E/k$ = 28.5± 0.2 K

τ_0= $1.6 \cdot 10^{-6} \pm 1 \cdot 10^{-7}$ s

A_{direct} = $2.85 \cdot 10^{-12} \pm 1 \cdot 10^{-14}$ $K^{-1}Oe^{-4}s^{-1}$

R^2 = 0.99997

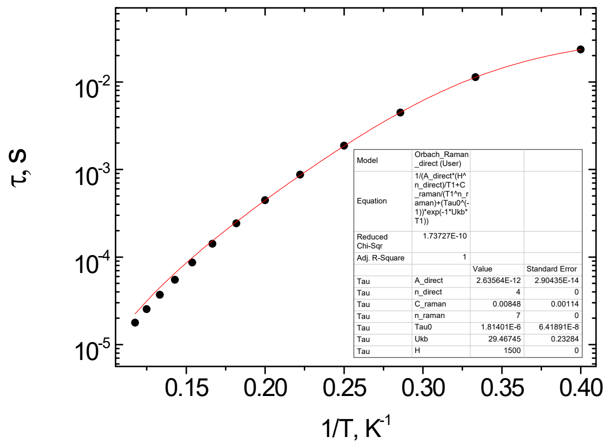

Orbach+Raman+Direct

$\tau^{-1} = \tau_0^{-1} \cdot \exp(-\Delta E/kT) + C_{Raman} T^{nRaman} + A_{direct} T H^4$

$\Delta E/k$ = 29.5± 0.2 K

τ_0= $1.81 \cdot 10^{-6} \pm 6 \cdot 10^{-8}$ s

C_{Raman}= 0.008±0.001 $s^{-1}K^{-nRaman}$

n_{Raman}= 7 (fixed)

A_{direct} = $2.64 \cdot 10^{-12} \pm 3 \cdot 10^{-14}$ $K^{-1}Oe^{-4}s^{-1}$

R^2 = 1

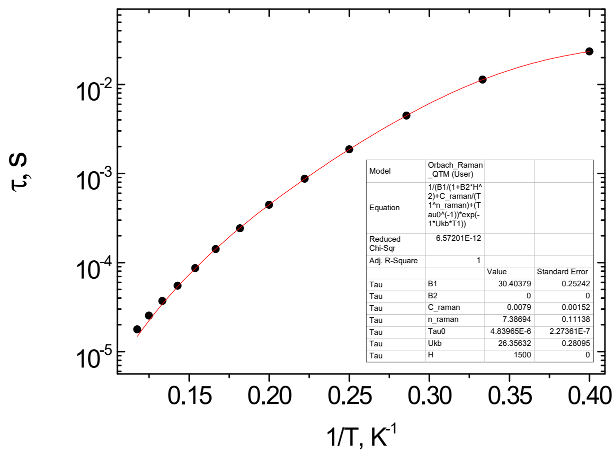

Orbach+Raman+QTM

$\tau^{-1} = \tau_0^{-1} \cdot \exp(-\Delta E/kT) + C_{Raman} T^{nRaman} + B$

$\Delta E/k$ = 26.4±0.3 K

τ_0= $4.8 \cdot 10^{-6} \pm 2 \cdot 10^{-7}$ s

C_{Raman}=0.008±0.002 $s^{-1}K^{-nRaman}$

n_{Raman}= 7.4 ±0.1

B = 30.4±0.3s^{-1}

R^2 = 1

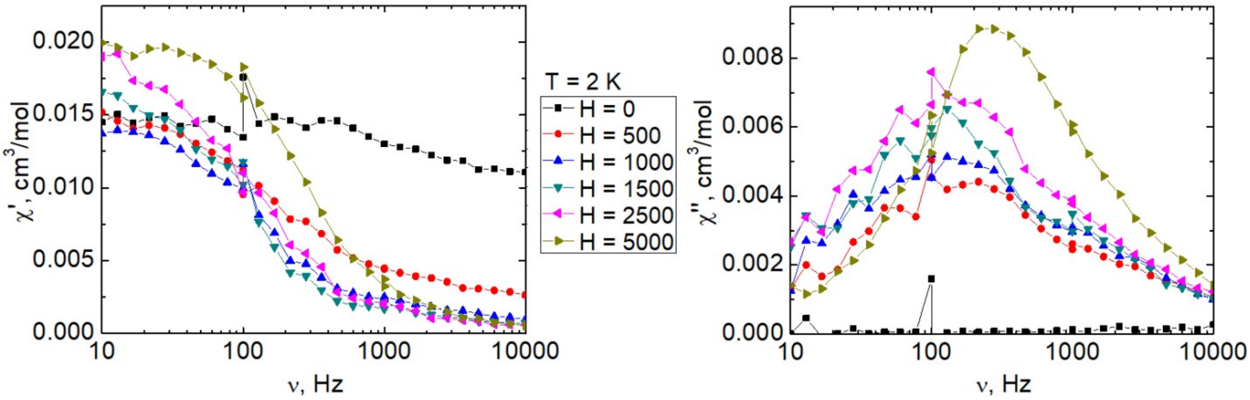

Fig. S22. Frequency dependencies of the in-phase (χ') and out-of phase (χ") components of the dynamic magnetic susceptibility of **1_Lu** at varied strength of the external static magnetic field and T = 2 К. Solid lines are visual guides.

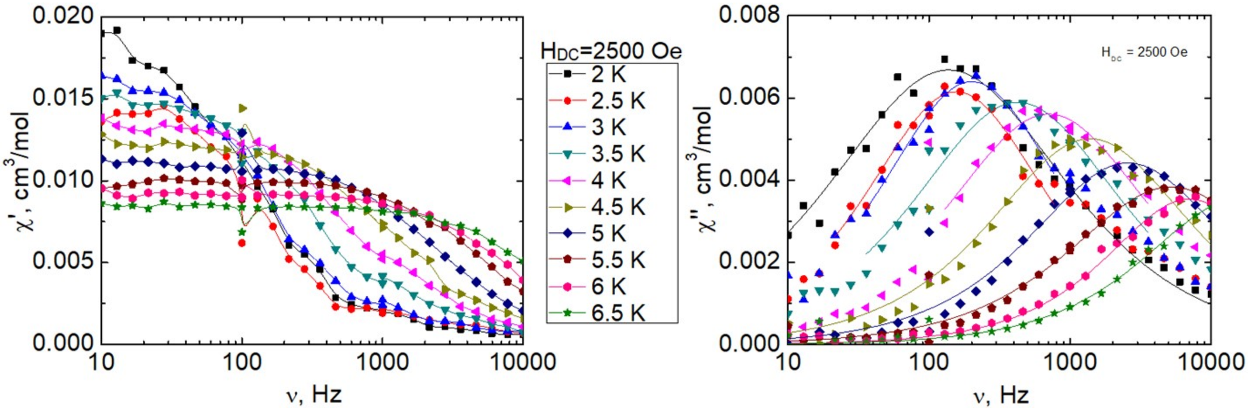

Fig. S23. Frequency dependencies of the in-phase (χ', a) and out-of-phase (χ", b) components of the dynamic magnetic susceptibility of **1_Lu** under optimal magnetic field 2500 Oe at various temperatures. Solid lines are visual guides (a), approximations by the generalized Debye model (b).

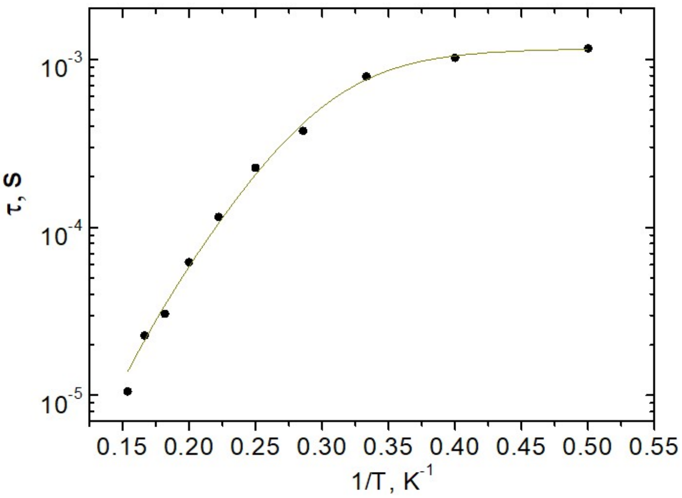

Fig. S24.τ*vs.* T^{-1} plots for **1_Lu** in 2500 Oe DC field. Solid line represents best fit by the sum of Orbach, Raman and QTM relaxation mechanisms.

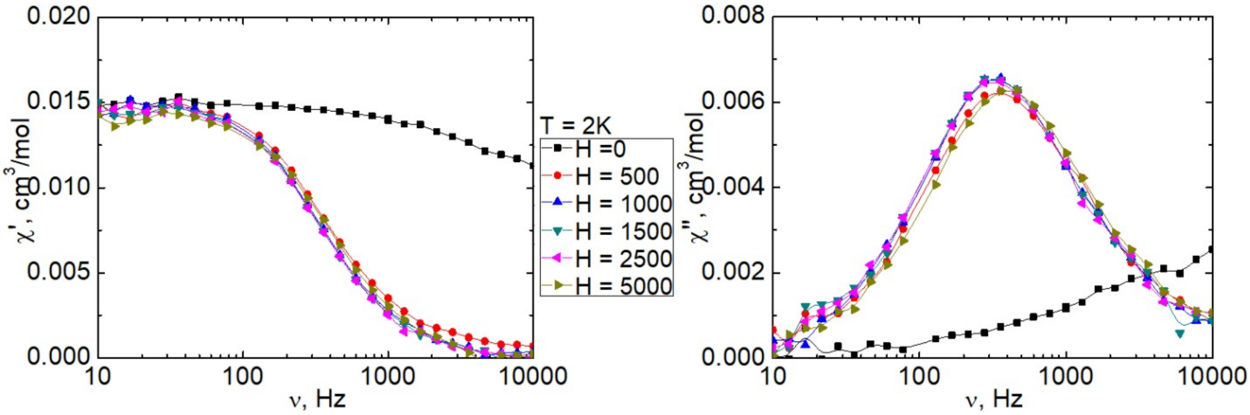

Fig. S25. Frequency dependencies of the in-phase (χ') and out-of-phase (χ'') components of the dynamic magnetic susceptibility of **2_Y** at varied strength of the external static magnetic field and T=2K. Solid lines are visual guides.

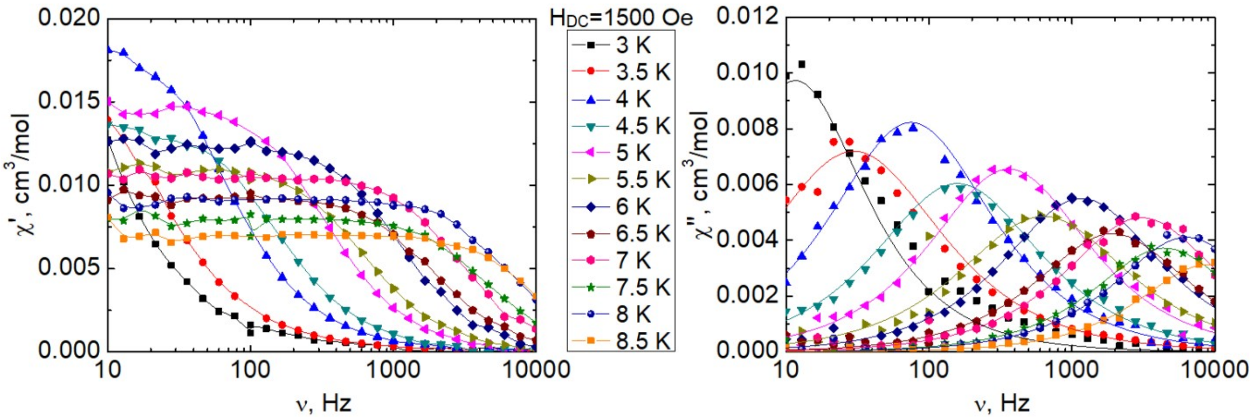

Fig. S26. Frequency dependencies of the in-phase (χ', a) and out-of phase (χ'', b) components of the dynamic magnetic susceptibility of **2_Y** under optimal magnetic field 1500 Oe at various temperatures. Solid lines are visual guides (a), approximations obtained by the use of generalized Debye model (b).

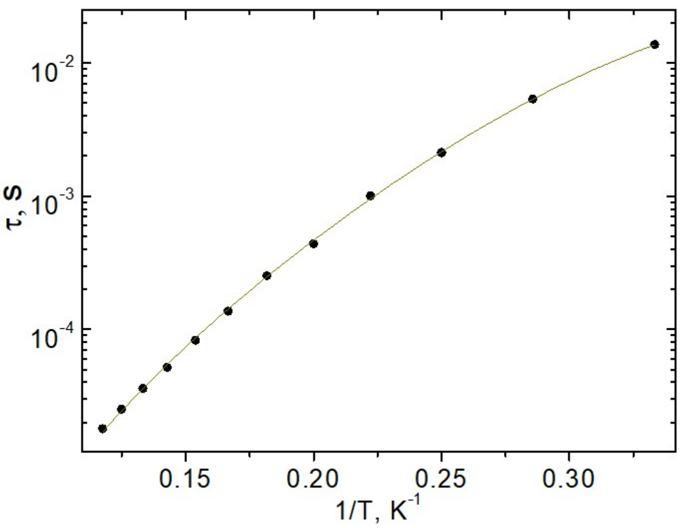

Fig. S27. τ*vs.* T^{-1} plots for **2_Y** in 1500 Oe DC field. Solid line represents best fit by the sum of Orbach, Raman and QTM relaxation mechanisms.

Table S6. Fitting parameters of magnetization relaxation for **3** and **4.**

Complex (*dc*-field, Oe)	Orbach+Raman+QTM				
	Δ_{eff}/k_B, K	τ_0,s	C_{Raman},$s^{-1}K^{-n\_Raman}$	$n_{\_Raman}$	B, s^{-1}
1_Lu (2500)	27 ± 3	$4.4 \cdot 10^{-7} \pm 4 \cdot 10^{-7}$	0.1± 0.1	7 (fixed)	860± 28
2_Y (1500)	35 ± 3	$1 \cdot 10^{-6} \pm 5 \cdot 10^{-7}$	0.040± 0.008	6.5 (fixed)	18± 5

Table S7. Known 7-coordinated Yb SMMs.

Complex / ***Nuclearity***	**Polyhedron**	**Δ_{eff}/k_B, K /** **(H_{dc})**	**[Ref.]**
[Yb(acac[2])$_2$(Q[3])]$_n$ (**1**)	Capped octahedron	40 / (1.5 kOe)	This work
YbL[I]·4H_2O / *Mononuclear*		16	2
Yb(trensal[II])‡ / *Mononuclear*		54.7†	5
[Yb_2(H_2cht[III])$_2$$Cl_4$($H_2O$)(MeCN)]·MeCN / *Dinuclear*		19.5(2)	8
YbL[IV] / *Mononuclear*		-§	9
YbL*[V]·3MeOH / *Mononuclear*			
{[Yb_2(DTE[VI])(H-DTE)(MeOH)$_2$]·2H_2O}$_n$‡/ *1D-polynuclear*	Capped trigonal prism	38.9†	1
[Yb($H_3L^{1,1,4}$[VII])]·2MeOH / *Mononuclear*		20.9†	6
[Yb{Ir(ppy[VIII])$_2$(dcbpy[IX])}$_2$(NO_3) (H_2O)$_4$]·Solv# / *1D-polynuclear*	Cappedtrigonalprism↔Pentagonalbipyramide	24.4	4
[Yb_2(OH){Ir(ppy)$_2$(dcbpy)}$_4$(NO_3)(H_2O)$_4$]·Solv# / *2D-polynuclear*	Pentagonal bipyramide	22.2	
Yb_2L[X]$_2$(depma[XI]$_2$)Cl_2 / *Dinuclear*		23.5	3
[Yb_2(NMP[XII])$_{12}$($PW_{12}O_{40}$)][$PW_{12}O_{40}$]#‡ / *Dinuclear*		11.84Δ	7
[Yb(BcrCOO[XIII])(acac[XIV])$_2$(H_2O)]$_n$# / *1D-polynuclear*		36	10
[Yb(H_3Bmshp[XV])(DMF)$_2$$Cl_2$]·DMF·1.5$H_2O$ / *Mononuclear*		14.5†	11
[Yb(H_3Bmshp)(DMF)$_2$$Cl_2$]·$H_4$Bmshp / *Mononuclear*		38.3†	

[I]L = fully (triply) deprotonated N[$(CH_2)_2$N=CH–R–CH=N–$(CH_2)_2$]$_3$N cryptand (R = m-C_6H_2OH-2-Me-5); [II]trensal = fully (triply) deprotonated 2,2′,2′′-*tris*(salicylideneimino)triethylamine); ‡No powder XRD data were provided for the studied samples; †Recalculated from cm^{-1};[III]H_3cht = mono deprotonated 1,3,5-cyclohexanetriol; [IV]L = *tris*(((3-formyl-5-methylsalicylidene)amino)ethyl)amine; §Δ_{eff}/k_B values were not determined since Orbach mechanism was not applied to fit relaxation times;[V]L* = triply deprotonated product of condensation of *tris*(((3-formyl-5-methylsalicylidene)amino)ethyl)amine with benzylamine; [VI]DTE = 1,2-bis(5-carboxyl-2-methyl-3-thienyl) perfluorocyclopentene); [VII]$H_3L^{1,1,4}$= triply deprotonated 2-[({2-[(2-hydroxybenzyl)amino]ethyl}{2-[3-(2-hydroxybenzyl)-2,2-dimethylimidazolidin-1-yl]ethyl}amino)methyl]phenol; [VIII]ppy = 2-phenylpyridine; [IX]dcbpy = 2,2'-bipyridine-4-carboxyl-4'-carboxylate; #Magnetic behavior of these complexes is governed by Yb^{3+} due to diamagnetism of the involved cations of heterometalls;[X]L = doubly deprotonated N^1,N^3-bis(salicylideneimino)diethylenetriamine; [XI]depma$_2$ = dimerized 9-diethyl-phosphonomethylanthracene; [XII]NMP = N-methyl pyrrolidone; ΔThis value was obtained for the Lu-diluted sample;[XIII]BrcCOO = (η_6-benzoate)tricarbonylchromium; [XIV]acac = acethylacetonate (pentane-2,4-dionate) anion; [XVI]H_3Bmshp = mono deprotonated (2,6-bis[(3-methoxysalicylidene)hydrazinecarbonyl]-pyridine).

References

1 M.A. Yatoo, G. Cosquer, M. Morimoto, M. Irie, B.K. Breedlove and M. Yamashita, *Magnetochemistry*, 2016, **2**, 21;

2 C.D. Buch, D. Mitcov and S. Piligkos, *Dalton Trans.*, 2020,**49**, 13557;

3 Q. Zou, J.-C. Liu, X.-D. Huang, S.-S. Bao and L.-M. Zheng, *Chin. Chem. Lett.*, 2021, **32**, 1519;

4 K. Fan, S.-S. Bao, R. Huo, X.-D. Huang, Y.-J. Liu, Z.-W. Yu, M. Kurmoo and L.-M. Zheng, *Inorg. Chem. Front.*, 2020, **7**, 4580;

5 K.S. Pedersen, J. Dreiser, H. Weihe, R. Sibille, H.V. Johannesen, M.A. Sørensen, B.E. Nielsen, M. Sigrist, H. Mutka, S. Rols, J. Bendix and S. Piligkos,*Inorg. Chem.*, 2015, **54**, 7600;

6 M. Fondo, J. Corredoira-Vázquez, A.M. García-Deibe, J. Sanmartín-Matalobos, M. Amoza, A.M.P. Botas, R.A.S. Ferreira, L.D. Carlos and E. Colacio,*Inorg. Chem. Front.*, 2020, **7**, 3019;

7 J. Li, C. Yuan, L. Yang, M. Kong, J. Zhang, J.-Y. Ge, Y.-Q. Zhang and Y. Song,*Inorg. Chem.*, 2017, **56**, 7835;

8 J.-D. Leng, J.-L. Liu, Y.-Z. Zheng, L. Ungur, L.F. Chibotaru, F.-S. Guo and M.-L. Tong,*Chem. Commun.*, 2013, **49**, 158;

9 C.D. Buch, S.H. Hansen, C.M. Tram, D. Mitcov and S. Piligkos,*Inorg. Chem.*, 2020, **59**, 16328;

10 A.V. Gavrikov, P.S. Koroteev, N.N. Efimov, Z.V. Dobrokhotova, A.B. Ilyukhin, A.K. Kostopoulos, A.-M. Ariciu and V.N. Novotortsev,*Dalton Trans.*, 2017, **46**, 3369;

11 D.-Q. Wu, D. Shao, X.-Q. Wei, F.-X. Shen, L. Shi, Y.-Q. Zhang and X.-Y. Wang,*Dalton Trans.*, 2017, **46**, 12884.

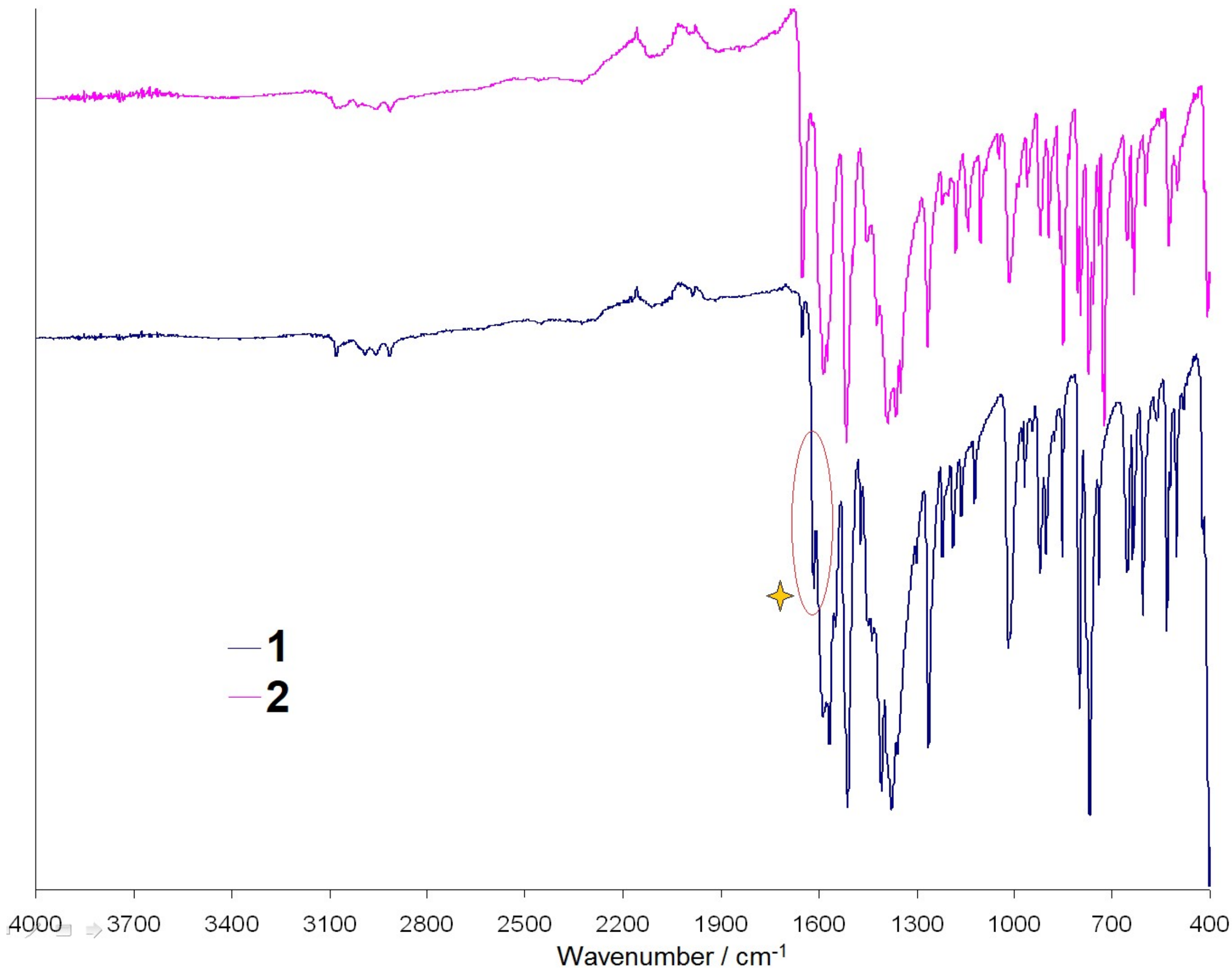

Fig. S28. IR spectra of **1** and **2** with specified band of high-energy asymmetric stretching vibration ofCOO(Q$^-$) groups.

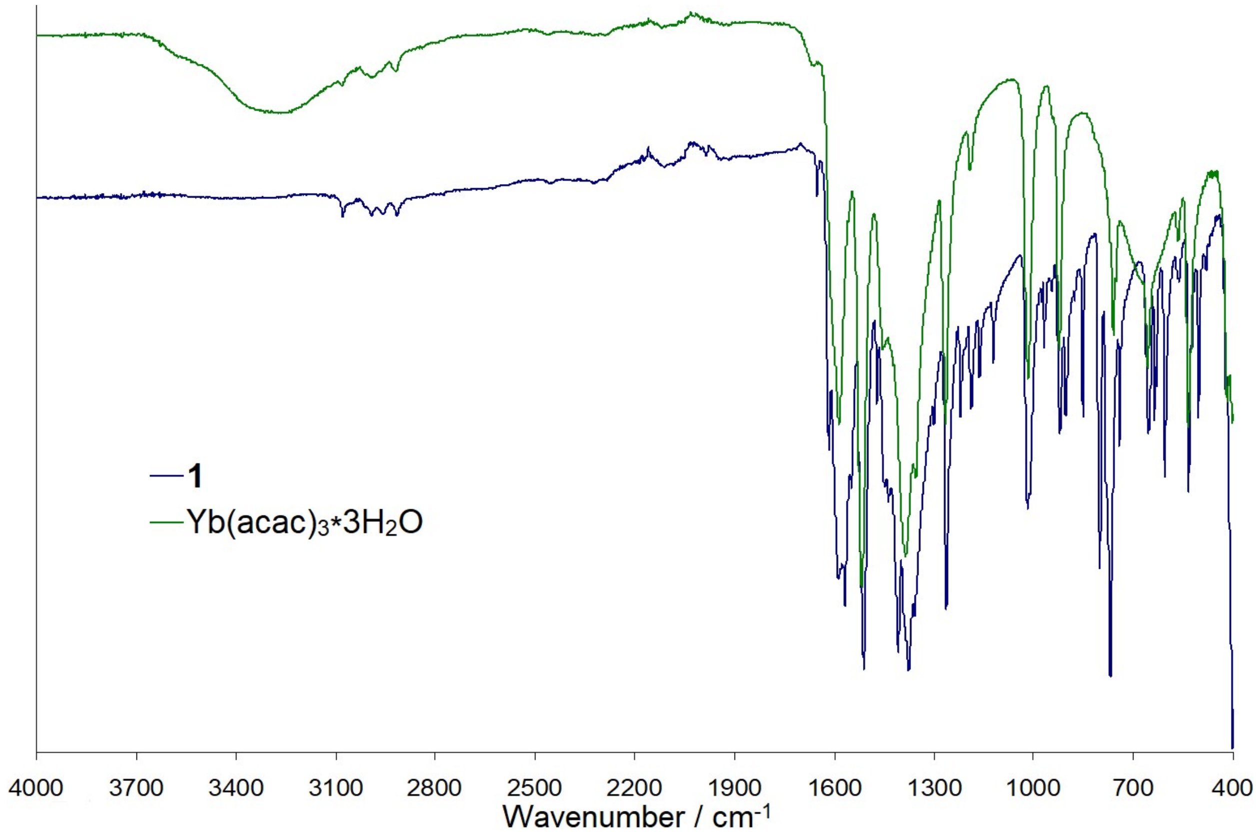

Fig. S29. IR spectrum of **1** compared to that of initial $Yb(acac)_3{\cdot}3H_2O$.

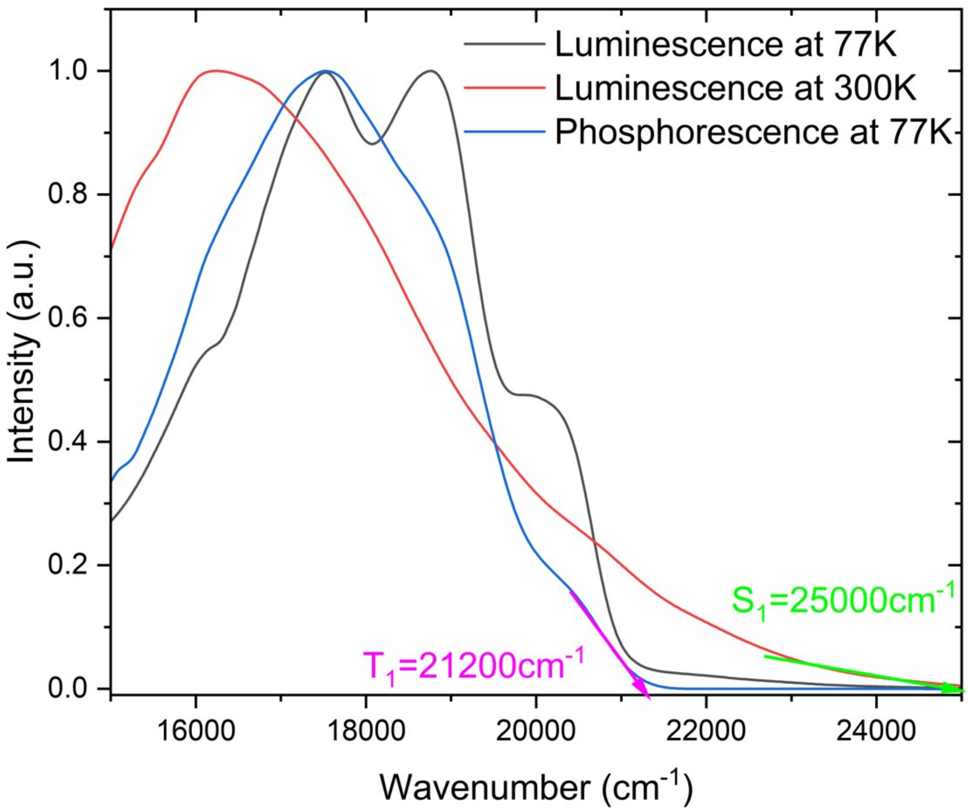

Fig. S30. Luminescence spectra in the energy representation for the **2_Gd** at temperatures of 77K and 300K.

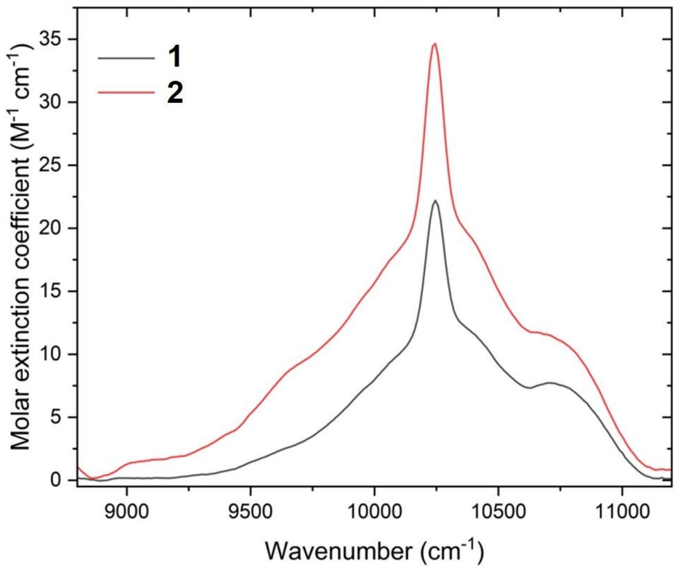

Fig. S31. Optical absorption spectra of solutions of **1** and **2** in DMSO.